Characteristics of Devonian Limestones in Plymouth, UK, a MW scale prospect for coastal aquifer energy.

Abbreviated title (<50 characters including spaces): **Coastal Aquifer Energy in Plymouth, UK**

Matthew T. Bailey[1*]

David Birks[2]

Rod P. Smith[3]

Jonathan Selman[4]

Orri S. Faulkes[1]

Eve Langman[1,5]

Nicholas Harper[6]

Billy J. Andrews[7]

Corresponding addresses:

1. University of Plymouth, Drake Circus, PL4 8AA *matt.baileyross@plymouth.ac.uk
2. Worley Consulting Ltd, The Quorum, Bond Street, Bristol BS1 3AE
3. John Grimes Partnership Ltd, Leonards Road, Ivybridge, Devon, PL21 0RU
4. Plymouth City Council, Ballard House, West Hoe Road, Plymouth, PL1 3BJ
5. Card Geotechnics Ltd, Tiverton, Devon, EX16 5HW
6. University of Exeter, Penryn Campus, TR10 9FE
7. Department of Earth Sciences, Durham University, Stockton Road, DH1 3LE

Keywords:

Ground sourced heating [and cooling]; aquifer energy; ATES; geothermal; Devonian Limestone; Karst

[PLEASE NOTE WE HAVE RETAINED SECTION NUMBERS TO ASSIST REVIEWING]

Abstract

Plymouth, UK, is a city underlain by a coastal karstic aquifer system, impacted by saline intrusion. The aquifer is being investigated as a source of ambient water for a city-wide heat network. Findings of aquifer-energy pumping tests are reported, highlighting the arising opportunities and challenges. The concept presented here deviates from typical aquifer energy systems, in that thermally spent waters are discharged directly to sea rather than reinjected into the aquifer, thereby negating the risks associated with reinjection wells and heat balance. However, at our study site in Plymouth, high sediment load persisted during pumping, likely sourced from either paleo-karst infill within the limestone, or buried tidal channels. We also present new structural data, which provides insights into the nature of the Plymouth Aquifer with respect to porosity architecture and fracture networks. Data are indicative of NNE-SSW trending structures which align with mapped faults and, porosity which is dominated by these fractures and cave systems within the limestone. Matrix porosity is low (mean: 5.2%), a result of diagenetic recrystallisation and post-diagenetic calcite precipitation in microfractures, indicating a low risk of irreversible salinisation. Development of the project at Plymouth could offer a blueprint for coastal aquifer energy systems elsewhere.

1. Introduction

1.1 The role of coastal aquifer energy in decarbonisation

Globally, space heating and cooling accounts for approximately half of final energy consumption and the building sector as a whole is responsible for 26% of global CO_2 emissions (IEA 2023). Demand is likely to increase in the future, driven by increased cooling requirements in a warming climate (Mastrucci *et al.* 2021). Heat pumps, powered by renewable electricity, offer a proven and scalable solution to decarbonising heating and cooling in the building sector, compared to alternatives such as hydrogen which are more expensive and more likely to be carbon intensive (Rosenow 2022; Billerbeck *et al.* 2024; Gao *et al.* 2026). Groundwater sourced heat pumps, when properly functioning, have a potential for high thermal efficiency and high yield, as they access thermally stable and large volumes of water and rocks in the subsurface.

Conventional aquifer energy storage systems (ATES) for seasonal space heating and cooling typically have a finite capacity to yield or absorb heat, which limits how much heat can be provided, unless a close balance between heat outputs and inputs is achieved. For most district heat networks currently under development in the UK, achieving a close balance between heat inputs and outputs is rarely practicable as annual heating demand typically exceeds annual cooling demand by a considerable margin. This represents a significant constraint on uptake of groundwater heating systems in the UK and globally (Birks 2019). Recently, there has been growing interest in the role that MW scale groundwater heating and cooling systems in flooded mines can play in addressing the issue of finite heating capacity (Banks *et al.* 2022; Birks 2023; Wyatt *et al.* 2025), including where flows exist at surface from passive discharge or active pumping (Bailey *et al.* 2016; Harrison *et al.* 2026).

A possible, hitherto overlooked, solution to this (heat balance) dilemma for ATES is the development of heating and cooling systems harnessing coastal aquifers where, subject to engineering and environmental considerations, the groundwater is discharged to the surface water environment rather than back into the originating aquifer. Where surface water discharge is possible the heat balance dilemma (Risk R4) and complexities associated with reinjection/recharge (Risk R2) are effectively negated (Figure 1). Consequently, where the heat balance constraint is removed and the complexities of recharge/reinjection avoided, groundwater heating and cooling systems based on abstraction from coastal water wells with surface water discharge could make a much larger contribution to district heat networks than conventional systems. Given that coastal wells draw seawater through the seabed and geology of the coastal fringe, abstracted groundwater temperature is less sensitive to seasonal variations than subsea pump sets, meaning that higher yields for a given flow rate can be sustained through colder winter periods.

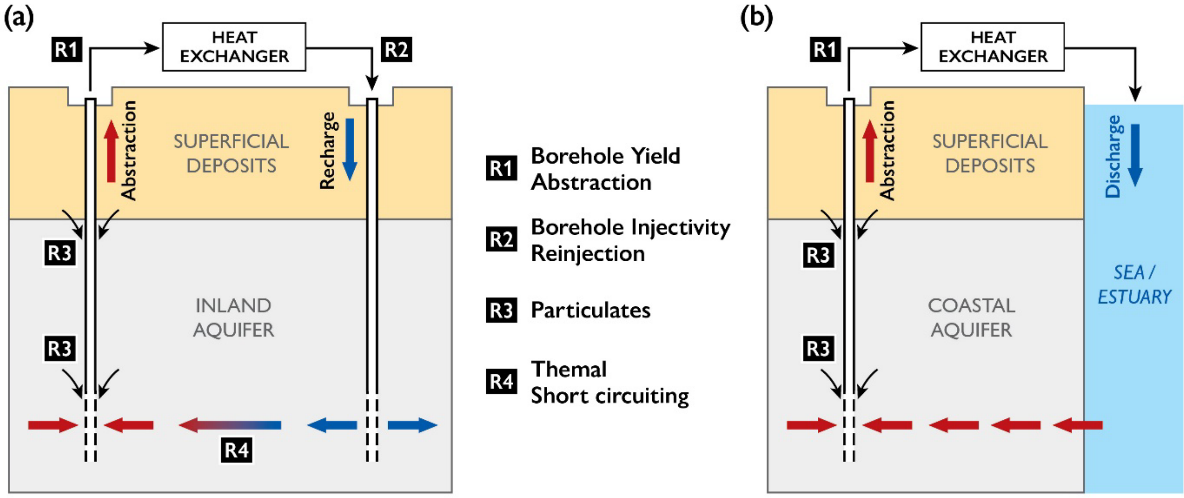

Figure 1 Aquifer energy system using an abstraction-reinjection well pairing (a), vs. a coastal aquifer energy system with coastal direct discharge (b), redrawn after Birks et al. (2022), showing key risks (R1-R4) associated with these systems.

Whilst it is true that, in coastal regions, aquifers can also be critical sources of fresh potable water for public supply and irrigation, facilitating economic growth and development (Custodio 2010; Klassen and Allen 2017; Nlend *et al.* 2018); pressures from overexploitation and contamination have, in many cases, led to deterioration of groundwater quality. Commonly, saline intrusion, which occurs due to overexploitation, results in the incursion of seawater into coastal aquifer systems, leaving water quality poor and unsuitable for many applications (Nlend *et al.* 2018; Ouarani *et al.* 2021; Heydarizad *et al.* 2023). This is known to have occurred in the mid to late 19th Century in the English city of Plymouth (Roxburgh 1983), with key wells along Union Street, between Stonehouse in the west and Cattedown in the east, becoming saline and abandoned. Documented, historical saline intrusion into the Plymouth Aquifer from the Elizabethan era into the 19th and early 20th century suggests that the freshwater resource within this coastal area is small. We propose that this presents a unique opportunity for heating and cooling purposes in coastal cities, where seawater is a significant component of the resource.

Heat pump systems utilising subsea intakes have also been found to afford promising solutions for the decarbonization of the heating sector, where seawater is utilised as a renewable heat source (Gille 2003). However, the cost of constructing and maintaining subsea pump intakes can be a limiting factor, where the high development cost may limit the economic viability for a typical district heating network. The concept of utilising coastal aquifers has gained traction within the desalination industry and is considered a valid proxy for large scale groundwater heating and cooling systems. Coastal wells are increasingly considered a viable proposition as a source of seawater for desalination plant where yields from wells are sufficient to meet demand (Ali *et al.* 2024). There are several reasons for this including:

- significantly lower development cost;
- reduction in permitting complexity, avoiding challenges of multi-landowner permissions and marine licensing;
- Reducing risk of storm derived sediment, detritus and biota entrainment.

Coastal aquifers therefore offer a unique, virtually limitless resource for high-yield heating and cooling applications, which we explore via a case study in the UK's 'Ocean City': Plymouth.

1.2 Scope of this study

Our aims are two-fold, **firstly** to capture ongoing efforts and lessons learned in the development of a megawatt-scale aquifer energy project, and **secondly** to present new geoscientific data on the Devonian Limestones of Plymouth which form the 'Plymouth Aquifer', to provide new insights into the role of structures and rock properties on the resource potential.

At the time of writing, considerable efforts by the local authority and its supply chain have been made to investigate the resource, as part of a 5th generation district energy system. This has included borehole investigations and large-scale abstraction tests, which have presented some unexpected challenges as set out in Development History and Learning. Significant resource potential exists, we discuss the theory and potential options for overcoming these obstacles, which have relevance to Plymouth and analogous sites elsewhere.

This study presents new structural and materials characterisation data for the Plymouth Aquifer, using a combination of field measurements, remote sensing and rock core microstructural analysis to characterise the Aquifer, identify flow paths and explore the role of porosity.

Low-temperature aquifer energy is the principal focus of this paper, though there is also unproven deep geothermal resource potential within the study area. Deep geothermal analogues are briefly explored.

1.3 Plymouth heat demands and networks

Plymouth is a Coastal city in the south-west of England, of 264,700 people (ONS 2022). It is a major port and regional urban centre. The 2017 Plymouth City-Wide District Energy Strategy (Nkonge 2017) identifies three high intensity heating and cooling demand clusters which could benefit from heat networks: the city centre, Devonport Dockyard and Derriford Hospital; the first two of which are located on the coastal fringe and have megawatt-scale heating demands (Nkonge 2017). This study recommended two district energy opportunity areas and informed the adopted Plymouth & SW Devon Joint Local Plan policy, requiring connection to a heat network within these areas.

Notwithstanding the challenges of aquifer energy heat balance, the impacts of climate change are projected to increase cooling demands. A 2026 study by Chinello and colleagues estimated that between 2022 and 2030, cooling demands in Europe will grow by 20% (630 TWh) for the residential sector and 27% (548 TWh) for the service sector (Chinello *et al.* 2026). Such an increased cooling demands during warmer weather places increasing pressure on heat networks to source adequate coolth, with shallow aquifers providing arguably the most reliable and sizeable thermal reservoir.

In our case study city of Plymouth, the largest cluster of high-heat demand wards are positioned above or in very close proximity to a karstic aquifer system, referred to herein as the Plymouth Aquifer, which could theoretically meet this demand at appropriate abstraction rates. In September 2024 the Council approved a strategy which supports the zonal approach to the heat network roll out in Plymouth including the procurement of a development partner to take forward the proposals to delivery. This follows significant work with and support from the Department for Energy Security & Net Zero. Heat Network zoning was originally set out in the Energy Act 2023, giving the government powers to establish zones. Plymouth City Council was selected by the Department of Energy Security & Net Zero (DESNZ) as one of 28 cities to be part of the government's Heat Network Zoning Pilot Programme and subsequently shortlisted under DESNZ's 'Advanced Zoning Programme' (AZP).

The Plymouth Zone Pilot in 2022 (As reported in Buro Happold and Plymouth City Council 2025) identified two preliminary heat network zones in Plymouth, one being the city centre/ waterfront area and another being in Derriford Hospital to the North of the City. The overall heat demand for all buildings required to connect within these strategic zones is approximately 250GWh/yr (annual average 28.5MW). There is presently no specified cooling demand. On 25th October 2024, the Department of Energy Security & Net Zero announced that Plymouth had been further shortlisted as one of 6 towns and cities which will be supported further, to move to delivery and will become the first heat network zones. At the time of writing, a Statutory Instrument on heat network zoning is expected to be in place later in 2026. A pre-Statutory Instrument zone boundary consultation for the two Plymouth proposed zones should also be completed in 2026.

2. Geology and hydrogeology

The Plymouth Aquifer comprises a heavily deformed, weakly metamorphosed Devonian reef limestone, thrust over siltstones and slates with interbedded limestones, which has undergone significant karstification. Geological setting and history of the locale is presented, setting the scene for the formation of the Aquifer and structural evolution relevant to creation of fluid pathways.

2.1 Paleo-geographic setting

The Mid-Late Devonian (Givetian-Frasnian) Plymouth Limestones were deposited within the Rhenohercynian Basin that extended from southern England in the west to Poland in the east (Woodcock *et al.* 2007). This formed as a backarc basin on the southern Avalonian paleo-margin due to subduction roll-back (Golonka 2020) following post-orogenic collapse of the Mid-European and North German-Polish Caledonides during the Early Devonian (Ziegler *et al.* 2002).

The northern limit of marine transgression onto the Early Devonian Old Red Sandstone Continent was significant enough during the Givetian and Frasnian to extend across both southern England (see Figure 3 of Bluck *et al.* (1992);Woodcock *et al.* (2007)) and western Germany (Garland 1997). Mixed carbonate-clastic sediments were deposited on shallow carbonate platforms flanked a deeper clastic basin to the south, but which was influenced by subduction-related volcanics that created a paleo-high where the carbonate reefs could grow. This resulted in deposition of the Plymouth Limestones in Devon (Bluck *et al.* 1992; Hamblin *et al.* 1992), and the ʻMassenkalk ʼlimestones in the Ruhr-Rhineland area of Germany (Garland 1997).

2.2 Tectonic history (paleo-reconstruction)

Variscan deformation

The Plymouth Limestones were deformed during the Variscan orogeny (Chapman *et al.* 1984). This prolonged Late Devonian to Early Permian orogenesis occurred due to Rheic Ocean closure and creation of Pangaea (Shail and Leveridge 2009), causing the Rhenohercynian Basin, along the southern Avalonian paleo-margin described above, to be deformed along its northern orogenic ‘front’ (Coward and Smallwood 1984).

The deformation in SW England Variscan fold-and-thrust belt (Sanderson 1979; Coward and Smallwood 1984) was north-west-directed and involved oblique convergence (Gayer and Nemcok 1994). Part of the deformation was controlled by structural inversion (Hartley and Warr 1990) of the original east-west-striking extensional faults of the Rhenohercynian Basin faults (Holdsworth 1989).

This NNW-directed Variscan oblique convergence (Alexander and Shail 1996) occurred during the Mid-Devonian to Carboniferous (Dodson and Rex 1970; Holder and Leveridge 1986). This resulted in thrusting, folding and associated low-temperature regional metamorphism (~250-400°C) (Coward and McClay 1983; Warr *et al.* 1991) until the latest Carboniferous (~312-305Ma) (Shail and Leveridge 2009). The deformation was partially controlled by East – West trending faults across SW England (Leveridge and Hartley 2006; Harper 2013). These former extensional fault zones from the Rhenohercynian Basin were reactivated as thrust/reverse faults during regional NNW-SSE contraction (Hartley and Warr 1990; Shail and Leveridge 2009).

As NNW-directed Variscan stresses throughout SW England were obliquely oriented to E-W-trending faults (Alexander and Shail 1996), kilometric-scale, regional NW-SE-trending, steeply-inclined faults were likely generated initially to accommodate and transfer the strike-slip component of the oblique contractional stresses before later cross-cutting the thrusts to accommodate strike-slip deformation (Dearman 1963). This movement caused fault reactivation, with the rocks moving to the right relative to each other (e.g., Sticklepath Fault Zone across the Dartmoor Granite) (Peacock *et al.* 1998; Nixon *et al.* 2011). Displacements on other cross-cutting faults range from millimetres to kilometres (Peacock *et al.* 1998; Harper 2013).

Although there are different tectonic models for Variscan deformation (Dearman 1963; Sanderson 1979; Coward and Smallwood 1984; Shail and Leveridge 2009), it is the Shail and Leveridge (2009) 'thick-skinned' tectonic model that agrees best with the deep seismic survey data available from across SW England (see Brooks *et al.* (1984)). The major mid-crustal regional reflector that was interpreted by Brooks *et al.* (1984) dips to the south at < 5°, lies at 12-15 km depth under Cornwall and south Devon, and may be equated to a surface at the base of the Cornubian Batholith (Harper 2013). This mid-crustal regional reflector model is further supported from findings of other seismic surveys, such as in the Rheinish massif, Germany, where this reflector has been interpreted to clip northwards (i.e. dip southwards) to 4-6 km deep (Leveridge *et al.* 1984).

The effect of this deformation upon the Plymouth Limestones is described by Chapman *et al.* (1984) and summarised in their tectonic reconstruction diagram (see Chapman et al., 1984). From both Chapman *et al.* (1984) and Shail and Leveridge (2009), the Plymouth Limestones were deposited in the Looe Basin and initially began to accommodate Variscan deformation during the latest Devonian to Early Carboniferous (Fammenian-Tournaisian). This occurred due to the obduction of the Normannian Nappe ophiolite, which was formed due to subduction roll-back (Shail and Leveridge 2009; Golonka 2020), and runs from the Lizard (south Cornwall) to Start Point (south Devon). As Variscan deformation progressed during the Carboniferous, the Plymouth Limestones were deformed by NNW-directed thrusts causing folding (Chapman *et al.* 1984) and then cross-cut by NNW-SSE-trending strike-slip faults that have accommodated multiple episodes of deformation (Shail and Leveridge 2009). Further, these limestones and other formations found in outcrop throughout South Devon have experienced very low-grade (anchizone) metamorphism (Warr 1995).

Post-Variscan deformation

Following Variscan orogenic deformation, extensional movements exploited the Variscan contractional structures during the Early Permian (~290 Ma to 270Ma) (Coward and Smallwood 1984; Shail and Alexander 1997). This extension was followed by Cornubian Batholith intrusions to produce (from west to east) the exposed Isles of Scilly, Land's End, Carnmenellis, St. Austell, Bodmin Moor and Dartmoor granites, which caused regional uplift and erosion (Coward and Smallwood 1984; Leveridge and Hartley 2006). These granites generate the geothermal energy potential across SW England. Further, as this granite batholith is suggested to have a lower crustal source with a mantle component (i.e. from beneath the Variscan mid-crustal reflector), the batholith may have a tabular form up to 9 km thick and may have exploited this mid-crustal décollement during post-Variscan extension (Shail and Leveridge 2009; Harper 2013).

The Permian deformation associated with granite intrusion is complex, as interpreted by Alexander and Shail (1996), and affects the NNW-SSE trending faults that cut through Cornwall and Devon, including the Plymouth Limestones. The Permian deformation involves firstly NNW-SSE extension with granite magmatism, followed by high-temperature mineralisation and ENE-WSW shortening. Also this deformation continued into the Triassic, with NNW-SSE shortening followed by low-temperature mineralisation and lastly ENE-WSW shortening (Alexander and Shail 1996; Shail and Alexander 1997).

Further, there is evidence for two regional unconformities in offshore basins close to Cornwall, one occurring around the Jurassic-Cretaceous boundary and the other during the Aptian (Early Cretaceous). McMahon and Turner (1998) suggest that the Jurassic-Cretaceous boundary unconformity relates to an uplift event around the Cornwall and Devon, whilst the Aptian unconformity relates to rift-flank uplift during the initiation of the Bay of Biscay sea-floor spreading.

The latest faulting event occurred during the Mid-Cenozoic (~40 Ma to 30 Ma) and caused both right-lateral and left-lateral reactivation on some faults (e.g., Sticklepath and Porthtowan Fault zones) (Peacock *et al.* 1998; Nixon *et al.* 2011; Harper 2013). These faults are modelled to be geothermal fluid flow conduits that crosscut the heat-producing granites (Law *et al.* 2019; Cotton *et al.* 2020; Farndale *et al.* 2022) and are targets for Enhanced Geothermal Systems in South West England.

Further, NNW-SSE-trending faults, which are parallel to these described here, cross-cut the Plymouth Limestones and the Cornelian Batholith (Dearman 1963). It is possible that these faults cut down to the underlying granite to the north of Plymouth and so could provide a geothermal fluid flow conduit into the Plymouth Aquifer at depth, as is modelled to be the case in Cornwall. However, this is an area for future investigation.

Structure

There is relative paucity of information regarding the facies present in the Plymouth Aquifer, with (Braithwaite 1967) providing a regional sedimentology overview of the different facies present from outcrops and quarry sections across South Devon, which includes the Plymouth Limestones as one of the Middle-Late Devonian carbonate reef mounds. In the Plymouth Limestones reef mound, (Braithwaite 1967) interpreted a mixture of thick-bedded stromatoporoid-algal reefs with corals dominating, fossiliferous micrites, bioclastic debris and thin-bedded limestones in shales (Figure 3). This agrees well with the facies described for the laterally-equivalent ‘Massenkalk’ Limestones in western Germany, where there is a mixture of fossiliferous microbes and spirits (Lippert *et al.* 2022).

As a result of the numerous deformation episodes to effect the region, there is little or no primary porosity in the Plymouth Limestones, with fracture porosity being common (Leveridge *et al.* 2002). Further, there is evidence for low permeabilities within the limestones, with flow only occurring along these fractures (Leveridge *et al.* 2002). The Plymouth Limestones have also been heavily karstified, with extensive cave systems known (Easterbrook and Smith 2018).

Consequently, further investigations of the Plymouth Limestones are required to understand what their fracture permeabilities are, what the effective porosities are within karstified limestones, and whether they have experienced dolomitisation and how extensive this process has been within the limestones.

Cross-cut by NNW-SSE-trending strike-slip faults that have accommodated multiple episodes of deformation (Figure 2). In section, the Plymouth Aquifer exhibits southerly dipping thrusted boundaries with Saltash Formation and Torpoint Formations as well as the faulted contacts with the Faraday Road Member and Prince Rock Member. The latter two are within the Plymouth Limestone formation, though the Plymouth Aquifer is known to extend into limestones of the Torpoint and Saltash Formation, with groundwater flow reported from slates to the north (Roxburgh 1983).

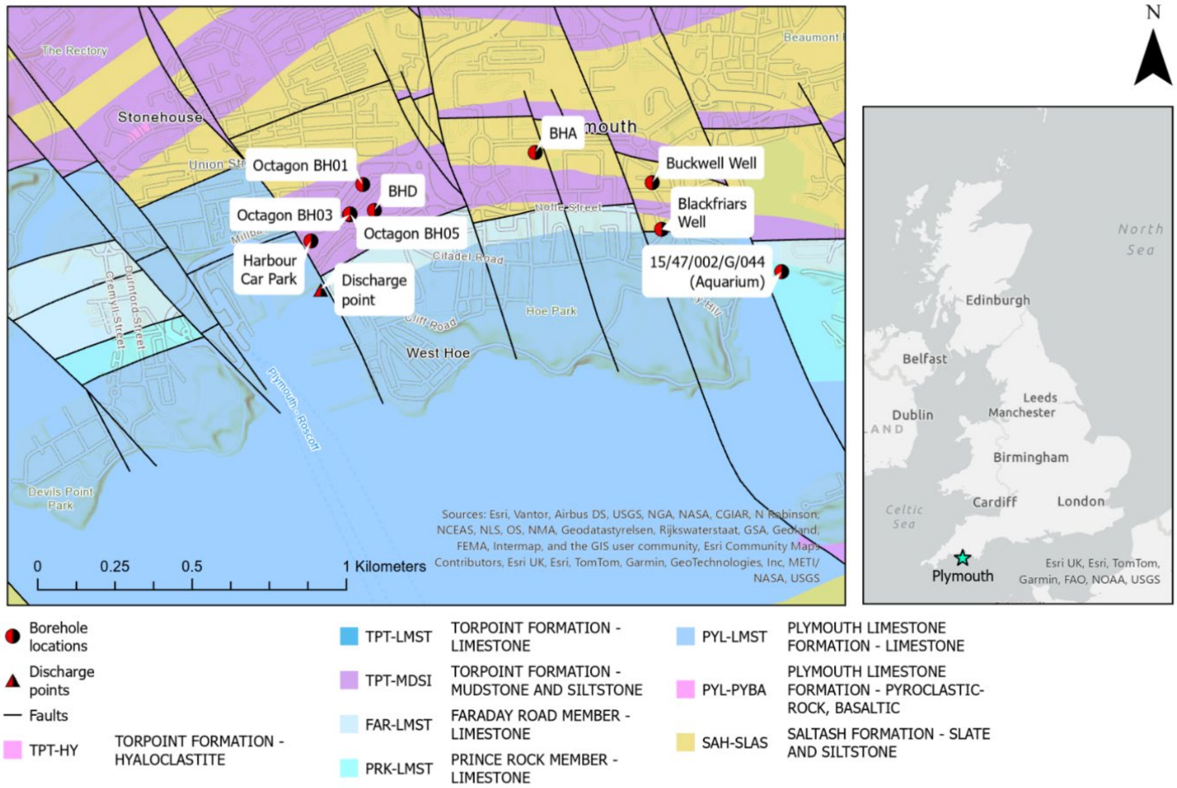

Figure 2 Geological map of the Plymouth waterfront. The map shows abstraction, monitoring and discharge locations from the 2022 and 2023 pumping tests reported herein. Geological Map Data BGS © UKRI 2026

The northern margin of the Plymouth Limestone is interpreted by Chapman *et al.* (1984) as being faulted, with a E-W trending fault affecting the boundary. However, the relationship between the topography and outcrop patterns at the northern thrusted margin of the Middle Devonian Limestones at Billacombe, east of Plymouth, shows gentle dipping to the south. They also describe a thrust that occurs at the base of the Plymouth Limestone that acts as a low angle contact with the succeeding formation. This along with the northern boundary has led to the entire boundary being interpreted as a low angle thrust, dipping to the south (Chapman *et al.* 1984).

Deformational fabric and structure of the Plymouth Limestone can be observed at outcrop along the Plymouth foreshore, as showing in Figure 3.

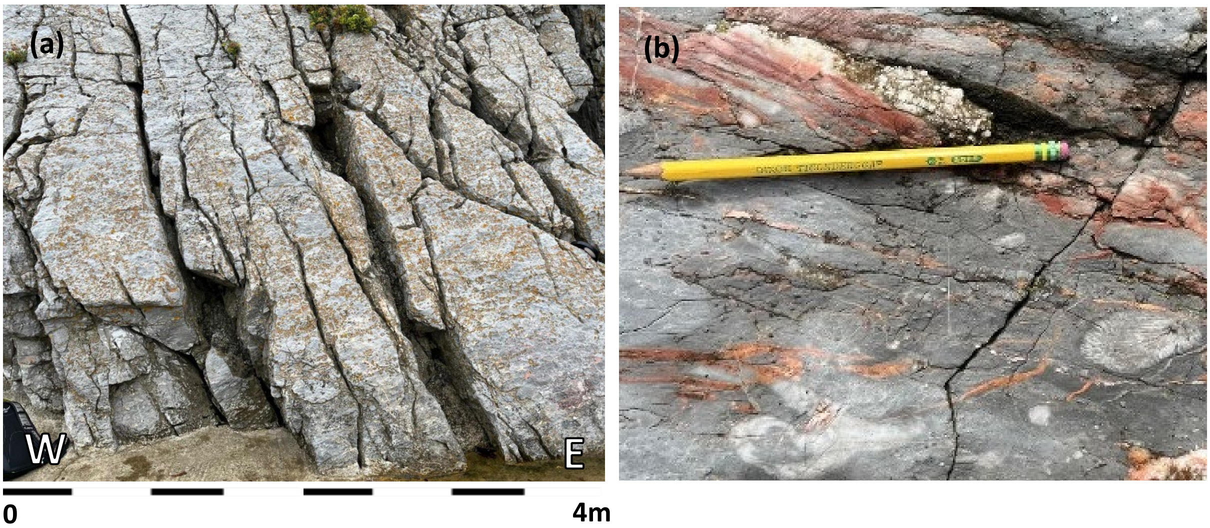

Figure 3 Photograph of the limestone at West Hoe (a), close up image with arrow pointing to a stromatoporoid (b). Also visible is the calcite rich red mudstone. Pencil for scale (b) @ Orri Faulkes, 2025

2.3 Aquifer energy potential

The Plymouth Aquifer, predominantly comprising limestones to the south of the city centre, is characterised by low matrix porosity and karst features, which are thought to extend 20m vertically due to historical sea level fluctuations (Roxburgh 1983). Development of the karst is thought to have occurred since the late Devonian, including both erosional and depositional processes (Easterbrook and Smith 2018) which have led to interconnected cave networks and paleo-infill. Roxburgh (1983) estimated that annual recharge within the limestone of the Plymouth-Stonehouse peninsula was of the order of $2.96x10^6$ m^3 per annum ($94ls^{-1}$), with significant additional inflows though to occur from slates to the north. Whilst historical abstractions remained a fraction of this flow (Roxburgh 1983), localised pumping would be expected to reverse the hydraulic gradient and draw in almost limitless volumes seawater along karst features and open discontinuities.

A notable yet poorly studied feature of the Plymouth Aquifer is the presence of submarine springs, partially in the regions of West Hoe and Devils Point/ Firestone Bay in Stonehouse. A significant upwelling, noted by Easterbrook and Smith (2018) is known as the Millbay Blue Holes, emanating from fissures at the base of a 30m high submerged cliff. This was discovered by police divers in the 1970’s and has not been investigated since, excepting for identification during aerial thermal imaging by (Roxburgh 1985).

The proposition of inflows into the Plymouth Aquifer would warrant further investigation, not only to confirm recharge areas to the north, but also explore the potential for influx of deeper, warmer water. Dartmoor Granite is located <10km to the NE of the city, with outcrops of the Bodmin Intrusion <20km to the NNW (i.e. along strike of the major faults within Plymouth) and may represent a possible source of deeper, geothermal water which could be exploited within the confines of the city.

3. Development history and learning

Investigation of the Plymouth Aquifer as a source of low carbon heat commenced in 2019, where the initial concept comprised four water wells to be utilised for abstraction and/or reinjection as part of an Aquifer Thermal Energy Storage (ATES) scheme, incorporated within a district heat network (Buro Happold 2019).

In 2020 two water wells were drilled to depths of 107m to 112m depth in the city centre, BHA and BHD, at locations shown in Figure 2. The reported geological sequence in BHA and BHD was similar, comprising dark grey to reddish brown mudstones to approximately 80m depth, overlying a crystalline, pinkish grey limestone (photograph of cuttings shown in Supplementary SI-1). Both water wells were lined with mild steel casing through the overlying mudstones to a depth of 82 - 84m and the lower sections of the boreholes left unlined with bottom hole diameters of 0.311m. Testing confirmed a very low yield in BHA of <1lsec^{-1} with a resulting drawdown of approximately 80m. In contrast, a relatively high yield was confirmed in BHD of 23lsec^{-1} with a corresponding drawdown of approximately 10m. At this flow rate velocity in the unlined portion of the borehole would be approximately 0.33msec^{-1} and the flow turbulent.

In 2021 Plymouth City Council commissioned an independent review of the drilling and testing works (WSP 2021) to obtain an objective assessment of the initial drilling and testing results. This assessment concluded that the relatively high yield confirmed in BHD was from a highly productive limestone unit within the Saltash/Torpoint Formation at depths of 80 – 90mbgl. Furthermore, this same productive limestone unit had been encountered at multiple locations in the general vicinity of BHD from drilling operations in the 19th and early 20th centuries, including off Martin Street as reported in the results section.

Whilst the testing records from BHA and BHD from 2020 did not confirm a seawater composition, evidence from previous drilling operations nearby indicated that groundwater pumped from BHD was likely to be saline. This assessment was consistent with a documented legacy of widespread salt - water intrusion into abstraction wells in the coastal fringe dating from the Elizabethan era (Worth 1890). The hypothesis that groundwater pumped from BHD might have a seawater composition was important because the requirement to reinject the water might be negated if this was the case, potentially paving the way for a surface water discharge.

The independent review (WSP 2021) also concluded that continued development groundwater as a source of low carbon heat for the heat network was **only viable** if surface water discharge was possible. The reasons for this were twofold, safety and economic viability. The primary safety consideration was whether reinjection of water at rates capable of supporting a MW scale contribution to the heat network (>100m^3/hour) was possible in a karst aquifer with a shallow water table (typically 2m to 5m below ground level) and numerous documented wells dating from the Elizabethan and Victorian eras, Figure . Specifically, whether reinjection could be achieved without causing flooding, subsidence or other damage to infrastructure. In 2022, structural damage reported following reinjection testing at a MW scale mine water project in South Tyneside had significant implications for the project and serves to illustrate the importance of considering the effects of reinjection. The primary economic consideration was related to safety, specifically, how many reinjection wells would be required to safely dissipate the recharge and where to place them.

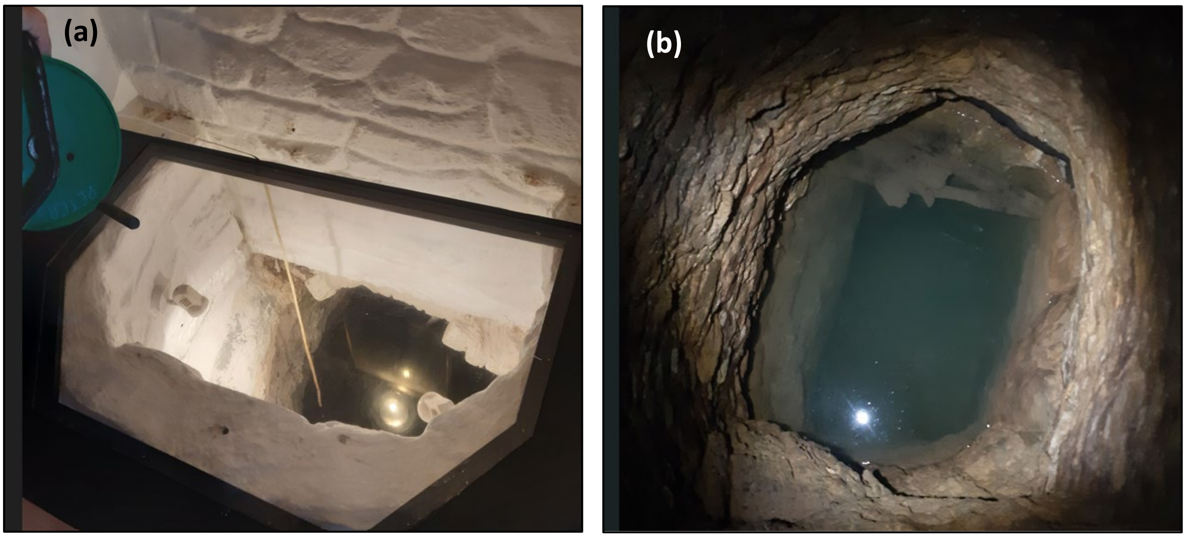

Figure 4 Photographs of Hand Dug Wells Dating from the Elizabethan Era. (a) Located close to the city bus station forming an ornamental feature in a local restaurant, (b) Located at Plymouth Gin Distillery on the Barbican (Blackfriars). @ David Birks, 2021

Having concluded that continued development of groundwater for the heat network was only viable with surface water discharge, it was necessary to demonstrate that consumptive abstraction (without recharge) could be undertaken without causing adverse environmental impact and, that surface water discharge was possible from an engineering perspective.

Early engagement with the regulatory authority (the Environment Agency) was undertaken ahead of the formal consenting process (Groundwater Investigation Consent, GIC) to obtain a consensus around the hypothesis that the freshwater resource was negligible and that BHD would very quickly discharge predominantly seawater after commencement of pumping. A specification for the testing of this hypothesis was subsequently developed in close consultation with the Environment Agency and formalised in the GIC (consent number 03070005).

The assumption that groundwater pumped from BHD would have a seawater composition underpinned the principal conclusion of the independent review, that development of groundwater as a source of low carbon heat was viable, contingent on a surface water discharge agreement being acceptable.

3.1 Testing Timeline & Configuration

Two testing campaigns were undertaken following construction of BHD and initial testing in 2020, the first was undertaken without filtration in 2022, the second and final test with filtration was undertaken in 2023. Figure SI-2 shows the general arrangement of the pumping test site.

2022 Pumping Test

Testing in 2022 was conducted with a 45kW electric submersible pump (Grundfos SP215/2), with the pump installed at a depth of 50mbgl, approximately 30m above the unlined section of the borehole. Following equipment tests conducted on 29th and 30th June, a step test was conducted on 4th July 2022. Flow rates for the step test are given in Table 1 and the drawdown response in the pumped source and offsite monitoring wells is shown in Figure 5.

At a flow rate of 70lsec^{-1} cumulative drawdown in the pumped well was 26.59m, with the pumped water level approximately 45m above the pump inlet at the end of testing indicating that this was a sustainable pumping rate. Drawdown responses were observed in three offsite monitoring wells with maximum observed drawdowns in Octagon BH01 of 3.7m, Octagon BH03 of 6.33m and a delayed response in the harbour carpark of 1.85m. Octagon BH01 was screened from 1 - 8.5mbgl through 5m thickness of alluvium and 3.5m into the Torpoint Mudstone. Octagon BH03 was screened from 4m to 9mbgl through 6.7m thickness of alluvium and 2.3m into the Torpoint Mudstone and the carpark borehole was screened from 1 - 6mbgl in made ground.

Figure shows that there was a progressive decrease in electrical conductivity over the test period from at 29.06mScm^{-1} and 21.98mScm^{-1} at the end of the test. This trend appears to be at odds with the progressively increasing concentration of total dissolved solids through the step test and subsequent testing, and is possibly due to increasing concentrations of suspended solids (e.g. silica), as the pumping rate and duration of pumping interval increased. It is possible that the decrease in electrical conductivity over the test period is indicative of an increased fresh/brackish component in the pumped discharge, but the increasing influx of suspended sediment would be a more plausible explanation (e.g. Holdich and Sinclair 1992). Corresponding laboratory derived measurements of electrical conductivity increased progressively through the test program attaining a maximum of 41,400µScm^{-1} on 5th July 2022 and were generally more consistent with concentrations of total dissolved solids (Table 2).

Table 1 2022 step test flow rates and drawdown observed in BHD

Step	*Flow rate (ls^{-1})*	*Water level at end of Step (mOD)*	*Cumulative drawdown (m)*
Standing water level	-	- 0.41	-
1	17.5	- 4.75	4.34
2	35.0	- 11.55	11.14
3	52.5	- 18.71	18.30
4	70.0	- 27.00	26.59

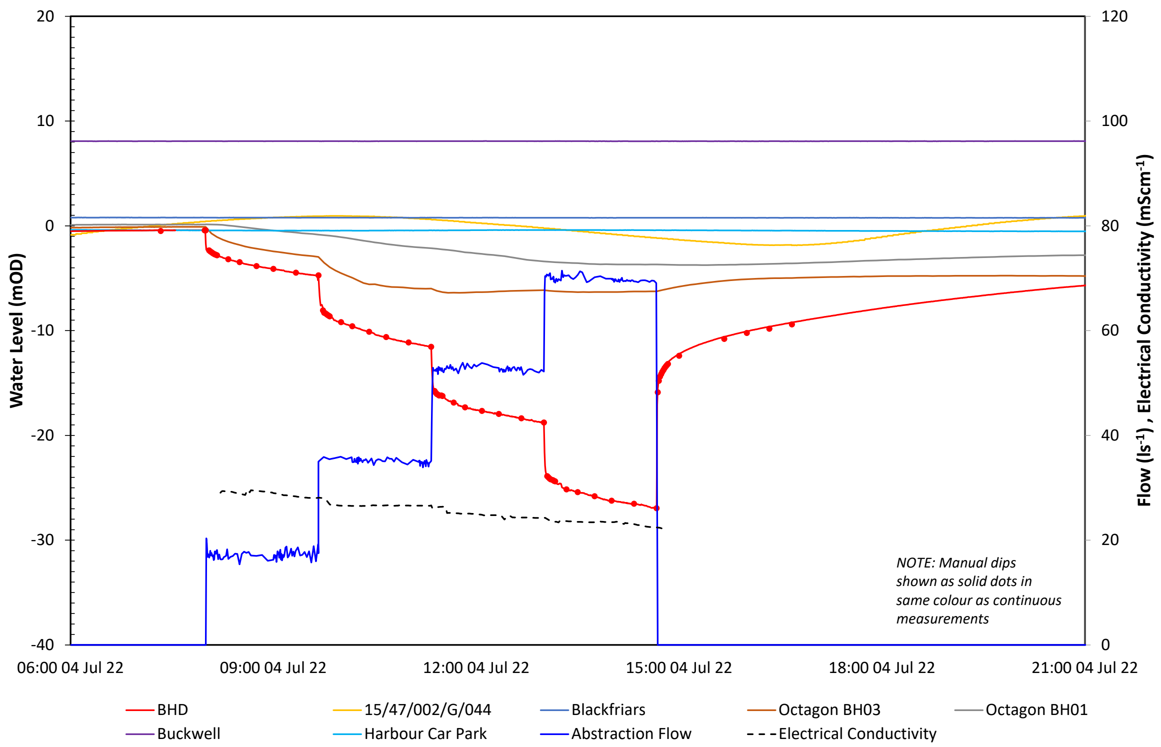

Figure 5 Drawdown response and conductivity trend for 2022 step test (adapted from WJGL 2022)

Total dissolved solids and suspended solids concentrations are given in Table 2. The pre - test sample obtained on 21st June 2022 is indicative of fresh water with a low dissolved and suspended solids content. Samples obtained during the step test on 4th July 2022 and subsequently showed a progressive increase in total dissolved solids, approaching a seawater composition as anticipated. Elevated concentrations of total dissolved solids (220mgl^{-1} to 391mgl^{-1}) persisted through the step test and all subsequent testing. Based on a total pumped volume (equipment tests, step tests and aborted constant rate tests) of 2,845m^3 and an average suspended solid content of 250mgl^{-1}, the total volume of solid removed during the 2022 test campaign is approximately 711kg.

The planned constant rate pumping test was not undertaken during the 2022 test campaign because the suspended solid content was causing a visual impact at the point of discharge, Figure 6.

Table 2 Abstracted water quality (Total Dissolved Solids & Suspended Solids), step test 2022

	Pre-test (22 June 2022)	*Step test (4 July 2022)*	*Aborted CRT (5 July 2022)*	*Low flow test start (6 July 2022)*	*Low flow test end (6 July 2022)*
Total dissolved solids (mgl^{-1})	84	23,300	30,600	31,600	43,500
Electrical Conductivity (µS/cm)	<100	24,510	41,400	39,600	37,000
Suspended solids (mgl^{-1})	21	257	391	273	220

Water temperature in the abstraction well remained stable between 14.26-15.42°C (mean 14.5, SD 0.24) between the 30 June and 18 July 2022, reflective of typical seawater temperatures at that time of year.

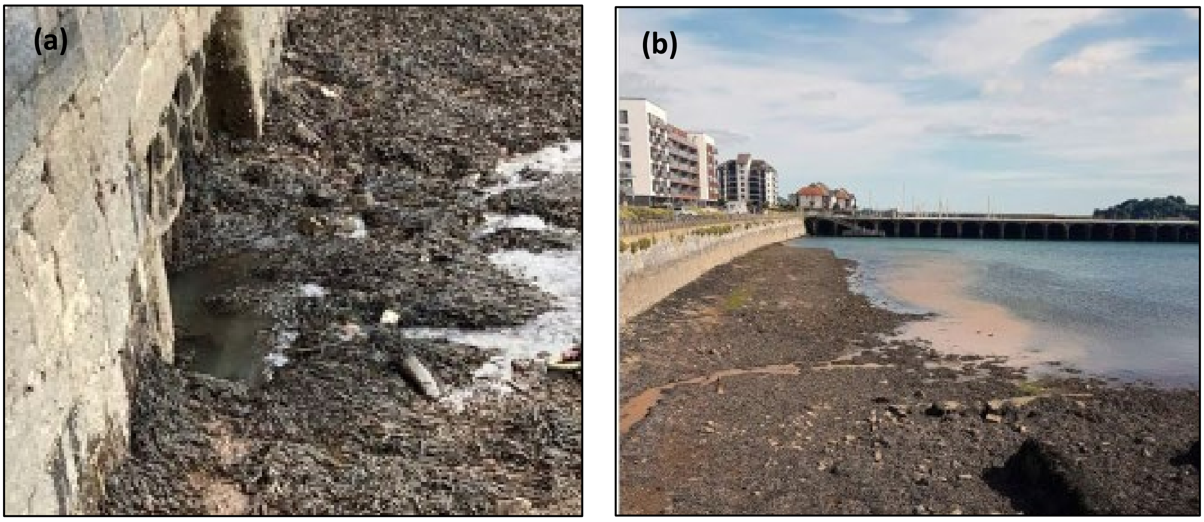

Figure 6 Visual impact of suspended solid content observed at discharge point, 2022 step test, 6th July 2022 15:40, culvert discharge at the start of pumping (a); 6th July 2022, 16:38 plume visible in harbour at the end of pumping (b) (WJGL 2022).

A review of the test procedures and results undertaken in June – July 2022 was undertaken the following autumn. This review concluded that key elements of the conceptual model, specifically a high yield and seawater composition were valid. However, the persistent suspended solid content was unexpected given that the borehole had been tested in 2020 at a flow rate of 23lsec^{-1} for a period of 4 hours and no issue with suspended solid content reported. It was concluded that the suspended solid was most likely an artefact of inadequate borehole development and that the suspended solid content was likely a transient issue which would resolve following a sustained period of clearance pumping. However, the drawdown responses in the offsite monitoring wells and conductivity trend observed during the step testing indicated a possible hydraulic connection between the unlined section of the borehole and the shallow alluvium. The site conceptual model was updated to reflect this understanding (Figure 7), and plans for a second test campaign with offsite filtration and an additional monitoring well screened only in the alluvium added to the scope.

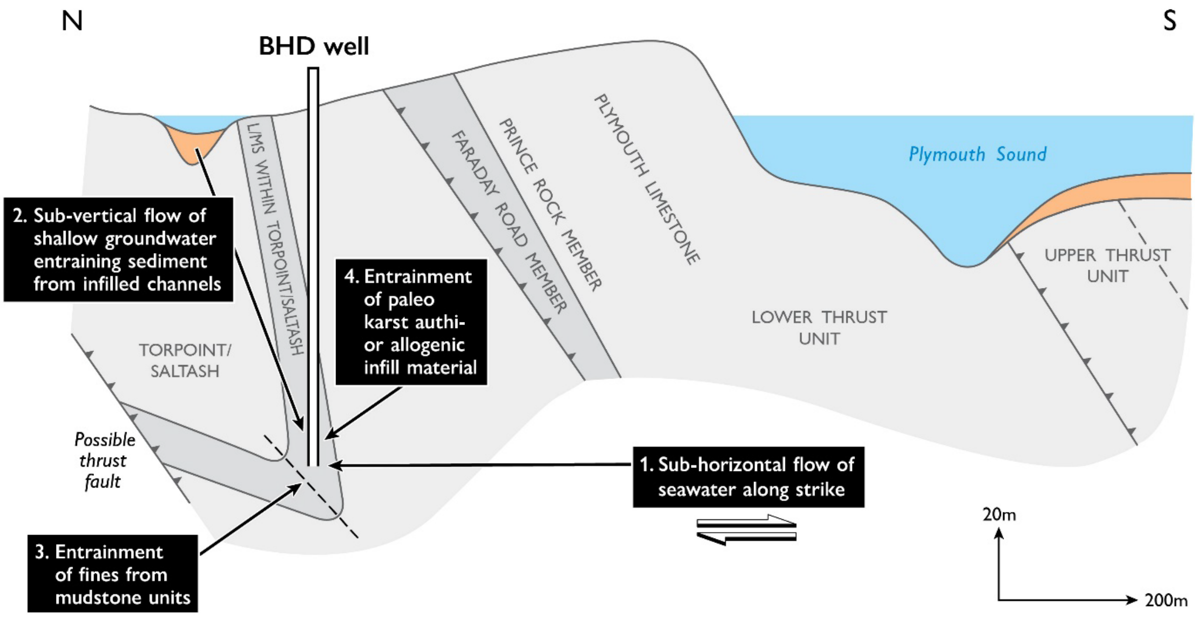

Figure 7 Conceptual site model for the Plymouth Aquifer showing potential sediment sources and flow paths. Note that the base of the BHD well is an open hole within a void.

3.2 2023 Pumping Test

Testing in 2023 was conducted with the same set up as 2022, with a 45kW electric submersible pump (Grundfos SP215/2) at a depth of 50mbgl, approximately 30m above the unlined section of the borehole. The discharge was passed through a multi-bag filtration system, Figure 9, sized for a maximum flow rate of 70lsec^{-1}.

The intention was to conduct clearance pumping at variable rates up to a maximum of 70lsec^{-1} for as long as necessary until the discharge ran clear and then to conduct a constant rate pumping test at 70lsec^{-1}. However, despite conducting multiple episodes of clearance pumping between 2nd May and 8th June 2023 the discharge continued to carry a high suspended solid content, and it was not possible to conduct the planned constant rate test. A hydrograph showing the clearance pumping is given in Figure 8 and the total volume pumped was approximately 40,257m^3. The total volume pumped in 2023 was approximately fifteen times the volume pumped in 2022.

Analysis of drawdown data the clearance pumping in 2023 is compared with that from the 2022 test campaign. Drawdown in the pumped well in the longest period of continuous pumping at 35lsec^{-1} (20 hours on 5th/6th June 2023) was approximately 23m and observed drawdown in shorter pumping intervals in response abstraction at 40 to 70lsec^{-1}, was typically between 15m and 20m, comparable with the drawdown response observed in 2022. Responses in Octagon BH01 and Octagon BH03 were 3.25m and 7m respectively and comparable with those observed in 2022. The drawdown response profiles in Octagon BH01 and BH03 were very similar to the drawdown profile in the pumped well, possibly reflecting the fact that these monitoring wells are screened in the alluvium and a few metres into the underlying mudstone. The drawdown response in Octagon BH05, screened in the alluvium only and constructed specifically for the 2023 test, shows a markedly different response, with a generally steady decrease from 0mAOD to -1.5mAOD over the entire test period. Drawdown response in the harbour carpark well appears to be independent of the pumping, showing diurnal and monthly variation, likely attributable to tides.

Measured electrical conductivity over the test period ranged between 15mScm^{-1} and 25mScm^{-1}, comparable with levels observed in 2022. The intermittent nature of the clearance pumping in 2023 means that there is no obvious trend in measured conductivity.

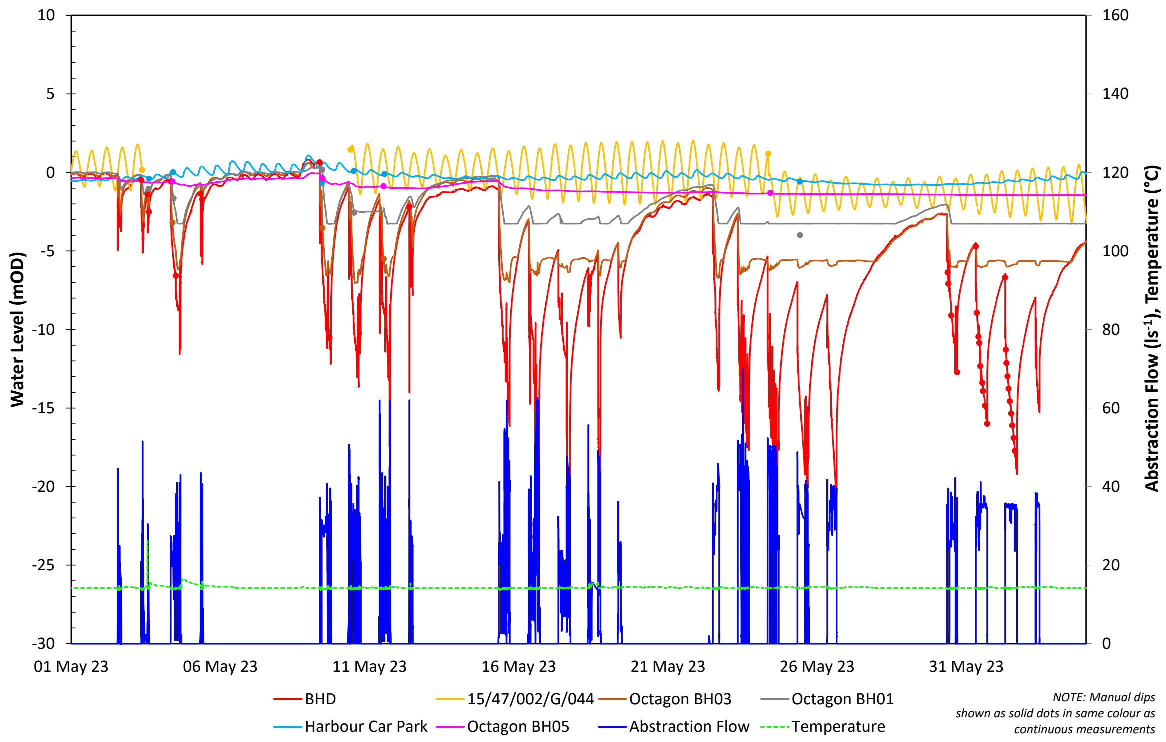

Figure 8 Drawdown response, step test, 2023 (adapted from WJGL 2023)

Clearance pumping typically followed a pattern where the flow rate was incrementally increased to a maximum of 70lsec^{-1}, which continued until the filters were became fully clogged and the testing had to stop to maintain a clear discharge after filtration and change out filter bags, Figure 9. Each pumping episode typically lasted 2 to 8 hours, and the maximum volume pumped in a single 24-hour period was 2,742m^3 on 5th June 2023. Each clearance pumping episode generally started with a clear discharge (zero suspended solid) and ended with a high sediment content, typically 2 to 5ml/l but occasionally higher (14ml/l on 4th May 2023 and 11ml/l on 10th May 2022). Assuming an average suspended solid content of 1ml/l, accounting for the fact that the discharge ran clear for most of each clearance pumping interval but became progressively cloudier in the final hours, the total mass of silt produced by the borehole is tentatively estimated to be 52T as a low density settled slurry (Figure 9a). This is based on a total pumped volume of 40,257m^3, average suspended solid content of 1ml/l and assumed density of the silty slurry of ~1.3g/cm^3 (e.g. Sills 1998), which would equate to approximately 20% solids at a dry density of 2.65 g/cm^3.

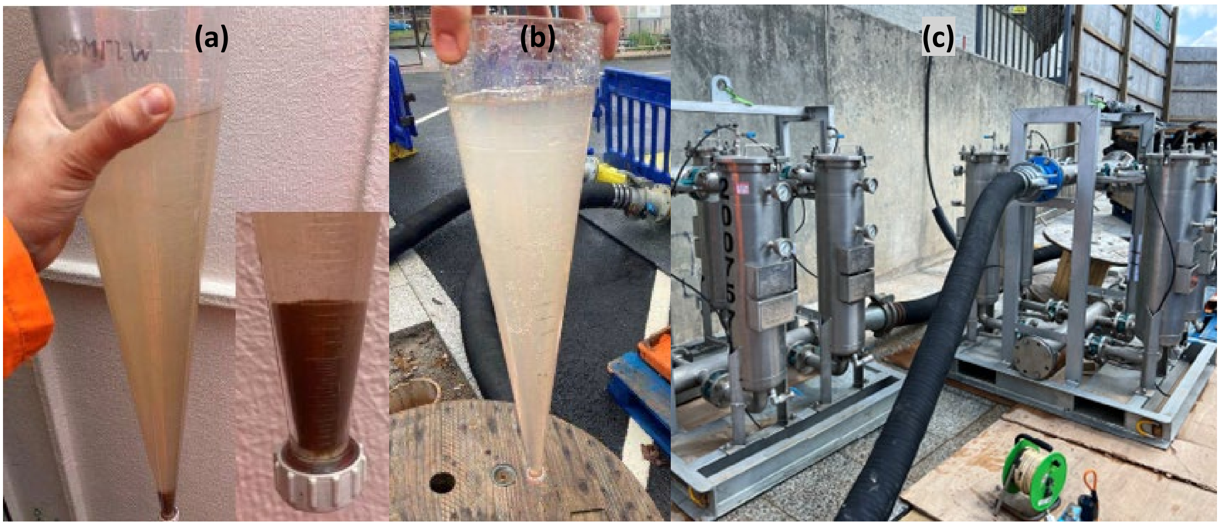

Figure 9 Suspended solids from clearance pumping interval 11 May 2023, (a) raw pumped water, 4ml/l; (b) after filter 2 (<0.1ml/l); (c) filtration unit @ David Birks, 2023.

Analysis of a groundwater sample obtained on 5th June 2023, during the longest period of continuous pumping, had a TDS concentration of 33,800mgl^{-1} and a chloride concentration of 14,000mgl^{-1}, representing a brackish-saline water. Water temperature in the abstraction well remained stable between 13.40-16.42°C (mean: 14.17, SD 0.25) between the 26 April and 14 June 2023 inclusive of the pumping phase, reflective of typical seawater temperatures at that time of year.

The decision to stop testing on 8th June 2023 was based on there being no indication that the suspended solid content would reduce with continued pumping and because of the high cost of plant (pumping and filtration equipment). There was also a concern relating to ground stability given that over 50T of sediment had been removed during the pumping and the piezometry indicating that the shallow alluvium was a possible source.

Prior to demobilising a downhole geophysical survey was conducted on 14th June 2023. The survey showed that the casing was intact to a depth of approximately 81mbgl and evidence for a large void between 94m and 96mbgl.

3.3 Pumping test implications and requirement for further investigations

Whilst testing and development works in 2022 and 2023 did not result in a viable groundwater source at the test location due to sediment load, it did confirm that key assumptions in the conceptual model were valid and that abstraction of seawater from the coastal aquifer could make a sizeable contribution to the developing heat networks, now or in the future.

Firstly, testing confirmed that very high yields could be attained from boreholes targeting the Plymouth Aquifer some distance inland from the coast. Secondly, that the freshwater resource within the coastal fringe has negligible resource value and that boreholes located adjacent to or close to the coastline discharge seawater. The second conclusion supports the hypothesis that surface discharge of water after heat exchange is a reasonable proposition, and this has significant implications for development/operating costs and the size and long–term viability of the heat source.

A possible model for development of the coastal aquifer in Plymouth is found at the National Marine Aquarium (NMA), which was included in the offsite monitoring in both (2022 and 2023) test campaigns. A 14m deep abstraction well at the NMA is equipped with a Grundfos SP17-5 submersible pump which runs for up to 2 hours daily to top up a large seawater tank. Flow rate during these daily pumping cycles is estimated at $5ls^{-1}$ and induces negligible drawdown relative to the natural tidal variation. It is conjectured that the NMA borehole should be capable of yielding significantly more than $5ls^{-1}$, potentially achieving yields of several tens litre/sec. Temperature measurements from the NMA (monitoring point 15/47/002/G/044) ranged between 14.5°C and 15.5°C (June-July 2022) and 11.7°C and 15.0°C (April-July 2023), consistent with sea temperatures at this time of year (Cefas 2026). Monitoring at the NMA serves to illustrate that, subject to careful site selection, relatively cheap, shallow water wells installed in the Plymouth Aquifer, where it outcrops along the city coastline, could yield prolific quantities of groundwater for a district heat network and that problems associated with suspended solid are not necessarily pervasive. Measured and published temperature data indicate that seasonal variation in abstracted water temperature is likely to range between 10°C and 16°C.

It is of note that the pumping tests carried out to date have been located in thin interbedded limestones within the Torpoint/Saltash formation, in similar locations to many of the main historical borehole water supplies and to the north of the Plymouth Limestone. Producing voids were encountered at depths currently around 50m below the base level of the Devensian Palaeo channel of the Tamar and Plym estuaries. Given this depth below a contemporaneous base level, these voids are unlikely to be speleo-genetically related to shallow karst voids within the coastal margins of the aquifer, even when factoring in relative uplift (Easterbrook and Smith 2018). Where karst has developed in the coastward Plymouth Limestone, the potential exists for mixed phreatic/vadose aquifer development. This is known to exhibit extensive anchialine cave development above and below current sea level and likely to have experienced significantly different infill history to the deeper void encountered in the pumping borehole.

Since completion of testing activity in June 2023, the entire dataset has been reviewed and, in parallel, targeted studies have been conducted by the University of Plymouth. These data are reported in the latter part of this paper and comprise a multi-scale evaluation of the Plymouth Aquifer, with the objective of furthering our understanding of the implications for development of coastal abstraction as a source of low carbon heat for the existing and future heat networks.

4. Methodology

To investigate the role brittle structures and karstification on the Plymouth Aquifer, we undertake a multi-scale analysis of the fault and fractures exposed along the Plymouth foreshore, Figure 10. This analysis captures features at three scales of observation: the macro-scale, which captures metre to 10's meter lineaments visible in areal imagery, meso-scale, which captures cm to meter lineaments using scanlines and window sampling, and finally micro-scale (mm to nm) structural features are captured using core samples. These scales were chosen as they broadly correspond to the classification method for carbonate system porosity featuring Karst (macro); stuctural features (meso) and matrix (micro), as set out in Cross and Burchette (2025).

Hydrochemical data are also presented from a range of sources to explore evidence of flow paths, both in terms of seaward migration of meteroric recharge and, inland migration of saline waters via structural features. Data include samples analysed as part of the 2022 and 2023 pumping tests; a summary of the methods are presented in this section.

4.1 Structural characterisation

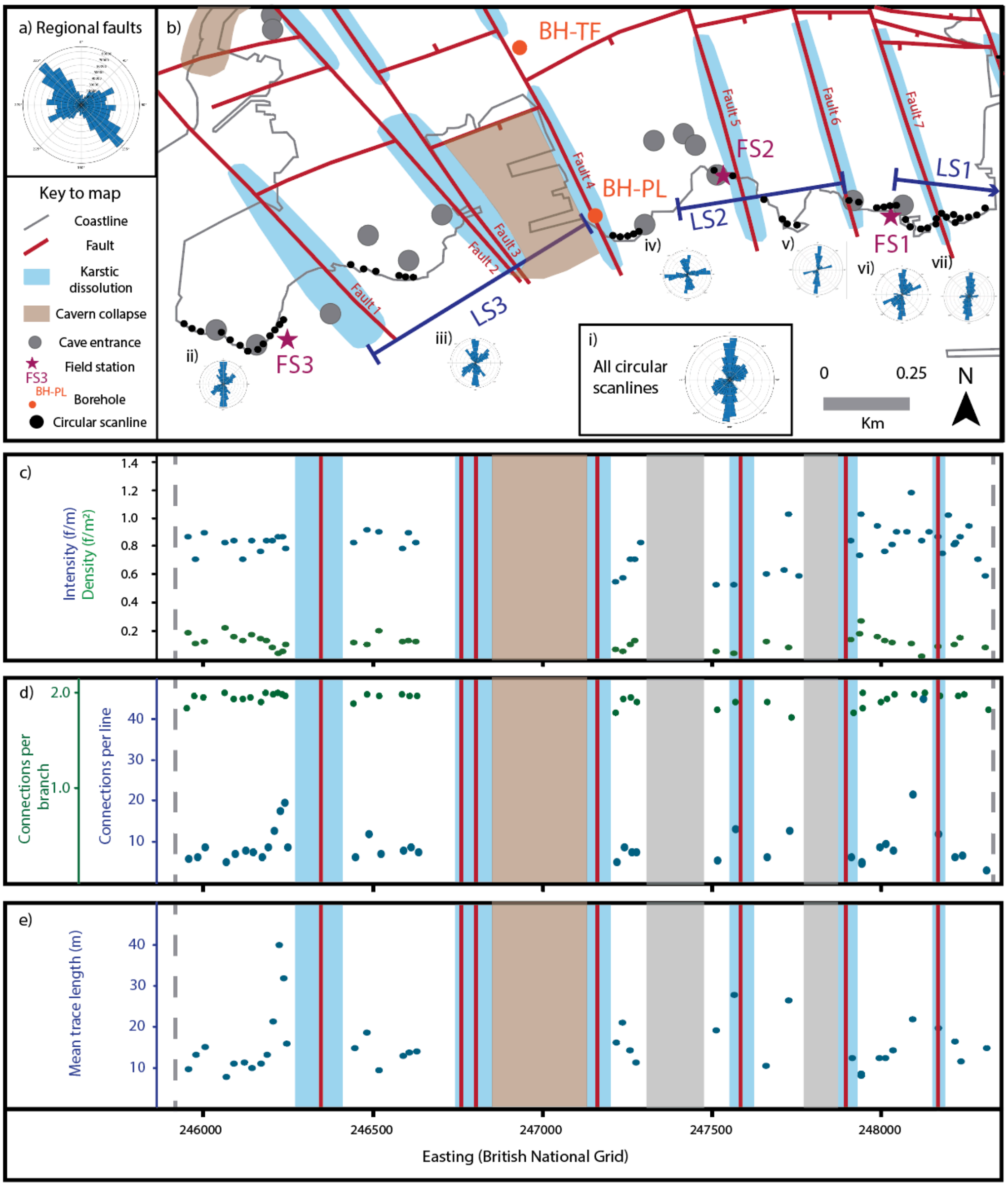

Figure 10 Fracture sampling locations and data extracted from the circular scanlines. A) Length weighted rose diagram for all "Faults" in the Plymouth geological map (UKRI 2026) which covers the study area, as well as nearby faults. B) sample localities and fracture orientation relative to the position of regional faults. Note how within the coastal fringe, the major NW to NNW trending faults show wide zones of enhanced karstic weathering and in places are associated with cave entrances. Length weighted rose diagrams for all circular scanlines (i), as well as scanlines between major faults (ii – vii) are also shown. Graphs of how c) fracture intensity and density, d) connections per line and connections per branch, e) mean trace length vary across the study area. Note how all network parameters remain favourable across the study area, with a small decrease between major faults 4 and 6.

Structural data were collected across a range of scales and compared with the regional faults on the published geological map by BGS (UKRI 2026). To capture macro-scale voids (>1 m), a linear scanline method was applied to the Plymouth Limestone exposed along the foreshore using Google Earth. Where a void was identified in the imagery, its position along the scanline together with the length and trend of the associated lineament was recorded. The spacing between adjacent voids was measured, using the path tool along a horizontal transect at mean high water level (Figure 10a). Linear scanlines are known to impart bias when not oriented at a high angle to the structures being sampled (e.g., Park and West, 2002; Priest, 1993). As the major structures are expected to strike NNW–SSE, whereas the scanlines trend E–W to ENE–WSW, orientation bias is not expected to significantly affect the sampling of major structures or voids. Consequently, no Terzaghi correction (Terzaghi 1965) was applied to our data.

Meso-scale discontinuities (i.e., tens of centimetres to ~10 m) were characterised using two complementary approaches: (1) circular scanline and window sampling of remotely sensed imagery, and (2) linear scanlines undertaken at three field stations (Figure 10a). A total of 50 circular sample windows were generated in QGIS by placing points along the foreshore where outcrop quality and extent were sufficient for reliable lineament mapping (i.e., avoiding areas of poor exposure or poor lighting). Circular sample areas were then created using the buffer tool, with most circles having a radius of 9.6 m (56%), decreasing to 6.3 m (38%) and 3.2 m (6%) where exposure was more limited. Within each sample window, lineaments were mapped from Google Satellite imagery (Google, 2026) in QGIS at a consistent mapping scale of 1:150 by a single interpreter. This ensured internal consistency throughout the study area and minimised interpreter bias so that along-strike variations reflected geological changes rather than differences in mapping style (Andrews *et al.* 2019).

Following digitisation, a combined circular scanline and topological sampling approach was used to characterise the fracture network within each sample window, allowing along-strike variations to be investigated (after: Watkins *et al.* 2015; Procter and Sanderson 2018). Circular scanlines reduce orientation bias and enable calculation of fracture intensity, density, and mean trace length by considering fractures intersecting the sample boundary (E-nodes) and fracture terminations within the sample circle (Mauldon *et al.* 2001; Rohrbaugh *et al.* 2002). Topological sampling characterises how individual fractures relate to one another within the network. The relative proportions of fracture terminations (I-nodes), abutting fractures (Y-nodes), and crossing fractures (X-nodes) provide a quantitative measure of network connectivity (Sanderson and Nixon 2015, 2018). Because I- and Y-nodes represent fracture terminations within the sample circle, these node classifications, together with E-nodes, can be used to calculate fracture intensity (Eq. 1), fracture density (Eq. 2), and mean trace length (Eq. 3) using the following equations:

$$\textit{Fracture intensity}\left(I,\frac{f}{m}\right)=\frac{N_E}{4r},\textit{where } N_E=\textit{number of E nodes}, r=\textit{radius of sample circle}\ [Eq\ 1]$$

$$\textit{Fracture density}\left(D,\frac{f}{m^2}\right)=\frac{N_I+N_Y}{2\pi r^2},\textit{where } N_I=\textit{number of I nodes}, N_Y=\textit{number of Y nodes } r=\textit{radius of sample circle}\ [Eq\ 2]$$

$$\textit{Mean trace length}\ (Tl,m)=\frac{N_E}{N_I+N_Y}\times\frac{\pi r}{2},\textit{where } N_E=\textit{number of E nodes}, N_I=\textit{number of I nodes}, N_Y=\textit{number of Y nodes}, r=\textit{radius of sample circle}\ [Eq\ 3]$$

The percolation threshold of a fracture network is defined as the critical point at which disconnected fractures become sufficiently connected to form continuous, system-spanning flow pathways (Balberg *et al.* 1984; Sanderson and Nixon 2018). Percolation threshold has been related to the number of connections per line (Equation 4), with a minimum structural limit of $C_L = 2$) (Balberg *et al.* 1984; Manzocchi 2002), and long-range connectivity occurring where $C_L = 3.57$ (Balberg *et al.* 1984).

$$Connections\ per\ line\ (C_L) = \frac{2(N_Y + N_X)}{N_L}, where\ N_Y = number\ of\ Y\ nodes, N_X = number\ of\ X\ nodes, N_L = number\ of\ lines$$ [Eq4]

Alternatively, particularly in networks containing a high proportion of censored fractures, the number of connections per branch can be used (Eq. 5), for which a critical threshold of Cb = 1.56 has been proposed (Sanderson and Nixon, 2018).

$$Connections\ per\ branch\ (C_B) = \frac{3N_Y + 4N_X}{N_B}, where\ N_Y = number\ of\ Y\ nodes, N_X = number\ of\ X\ nodes, N_B = number\ of\ branches\ [Eq5]$$

To complement the remotely sensed data, field measurements were collected at three limestone outcrops along the foreshore: east of Tinside Lido (FS1), the West Hoe area (FS2), and Firestone Bay (FS3) (Figure 10a). At each location, a minimum of three linear scanlines were completed to sample x-, y-, and z-orientations. For each fracture intersecting the scanline, spacing, trace length, orientation (dip and dip direction), discontinuity type (e.g., joint), aperture, and infilling material were recorded. Fracture spacing measurements from each scanline were used to calculate fracture intensity, which was classified according to (Bieniawski 1989). To compare network topology across observational scales, topological sampling, following the methodology described above, was also undertaken on three field photographs collected from the three field stations. Finally, datasets from all scales were integrated to assess the fracture network properties of the Plymouth Limestone and their implications for this coastal fringe aquifer.

4.2 Rock property analysis

Samples of Limestone were obtained from two core runs from the University of Plymouth archives. These runs were taken from a rotary cored borehole off Martin Street, and range from 23 - 25mbgl (Limestone in Torpoint Fm, BH-TF) and from a rotary cored borehole from the Millbay ‘Block B’ development taken from 2.5 – 5mbgl (Plymouth Limestone, BH-PL), as shown in Figure 10. Optical Microscopy (OM), Scanning Electron Microscopy (SEM), and porosity analysis using ImageJ were utilised to gain an insight into the samples’ fabric and microporosity. This includes two methods of sample preparation depending on the analytical technique used, summarised in Table 3. TF1 was split down into three replicates, one SEM sample (S-TF1), and the remaining two into thin sections (O-TF1-2). PL1 was split into 5 replicates, which in turn produced 4 thin sections (O-PL1-5), we were unable to obtain reliable SEM imagery for the PL specimens so this data is not presented.

Table 3 Data table summarising replicate types and quantities used in porosity analysis.

Sample ID	*Replicate*	*Replicate Type*	*Comments*
BH-TF	S-TF1	SEM sample	Split into 20 images for porosity analysis (Lmst1-20)
	O-TF1	Thin section	From 24mbgl (no set orientation)
	O-TF2	Thin section	From 25mbgl (no set orientation)
BH-PL	O-PL1	Thin section	Perpendicular orientation
	O-PL2	Thin section	Perpendicular orientation
	O-PL3	Thin section	Perpendicular orientation (polished)
	O-PL4	Thin section	Parallel orientation
	O-PL5	Thin section	Parallel orientation (polished)

SEM Preparation

Using an IsoMet1000 precision saw, S-TF1 was cut down to ~10mm in length, and 3-8mm in width. Any uneven texture was removed via sanding with aluminium oxide (Al_2O_3) and water (H_2O) to ensure the SEM could focus correctly. Samples were then dehydrated over a period of 24 hours before being secured to the top of the SEM stub using circular double-sided conductive tape. Prior to SEM analysis, S-TF1 was covered in a sputter coating of gold using the JEOL Smart Coater to improve conductivity and image resolution. Samples were then photographed using a JEOL Neoscope benchtop under vacuum conditions, utilising its automated focus, beam shift, stigma, SRT, and brightness functions.

OM Preparation

Representative samples of the Torpoint Formation and Plymouth Limestone were prepared as petrographic thin sections, to enable comparison between these two formations. Analysis was then undertaken using a digital camera enabled Nikon optical microscope to characterise their relevant properties, including pore connectivity, mineralogy, and porosity.

ImageJ Modelling

SEM images were analysed using ImageJ software to produce two-dimensional models to calculate percentage porosity area. Images were first turned into RGB colour types and separated into individual channels. The threshold tool was then applied to produce binary black and white images, enabling for the distinction between particles and pore space. Quantitative analysis was performed by setting the pixel size to "pixel^2", and average pore percentage area. Mean porosity values (% area) was calculated for S-TF1 only.

4.3 Hydrogeochemical analysis

Water quality analysis for samples collected during the pumping tests was undertaken by a third-party UKAS accredited laboratory (Socotec, Bretby, UKAS 1252 registration number). Samples for inorganic analysis were collected in 1L plastic containers and transported in cool boxes to the laboratory under a chain-of-custody procedure. Metals were analysed by Inductively Coupled Plasma, Optical Emission Spectrometry (ICP-OES, 'ICPWATVAR'), anion analysis (sulphate and chloride) by automated discrete colorimetric analysis ('KONENS'). pH, alkalinity and conductivity were measured using proprietary methods in accordance with BS 2690:1984:Part 109.

5. Results and discussion

5.1 Structural characterisation

The study areas is dominated by regional faults (Figure 10b), small-offset faults, fractures with no obvious offset along them (i.e., joints), and pink to white calcite veins (Figure 3). In all outcrops, the veins are closed and cross-cut by later faults and joints (Figure 3). As these veins do not provide pathways for groundwater flow and can only be observed at the cm to m scale, they were omitted from further analysis. Fracture lengths vary with the scale of observation (Figure 11a), ranging from 0.3 to 4 m (average = 1.3 m) at the field stations, 0.6 to 19.4 m (average = 6.0 m) from the circular scanlines, 19.2 to 13469.2 m (average = 1027.6 m) for regional faults. At each scale, fracture length distributions are highly truncated and contain relatively few censored fractures (Figure 11a). This indicates that many mapped fractures extend beyond the sample area and that their true lengths are substantially greater than those measured. This is supported by the higher mean trace length estimated from circular scanlines, which ranges from 3 to 40 m (average = 8.1m). Despite the effects of censoring and truncation, fracture lengths from all observational scales define a negative power-law relationship between length and normalised areal frequency (Figure 11a), suggesting that they represent a single fracture population.

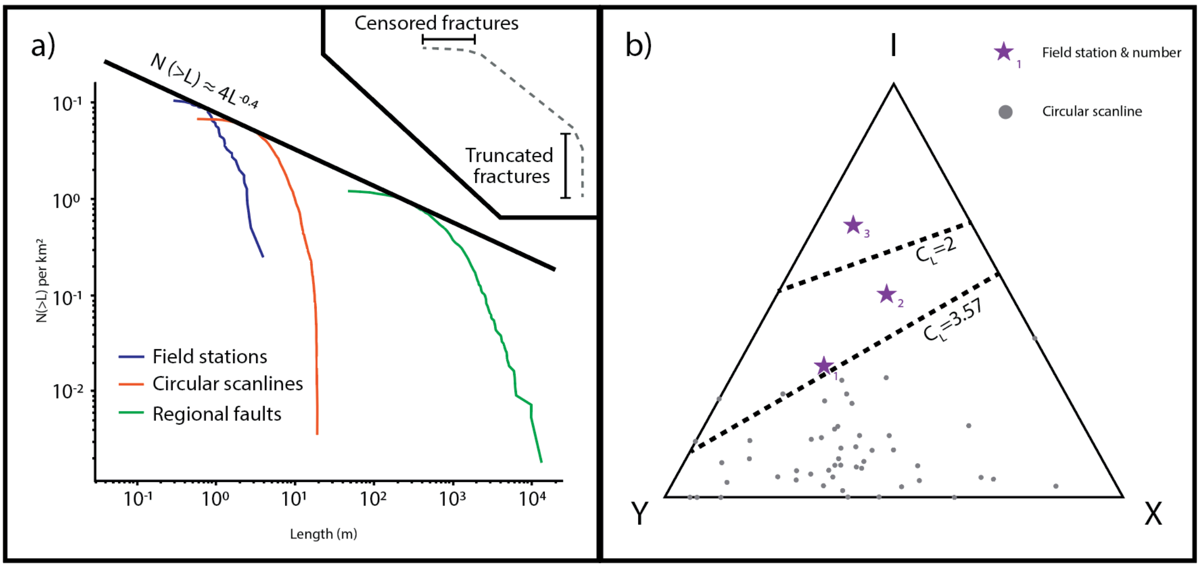

Figure 11 Length and topology data. a) plot of area-normalised cumulative fracture length distributions for all scales of observation. b) node triangle.

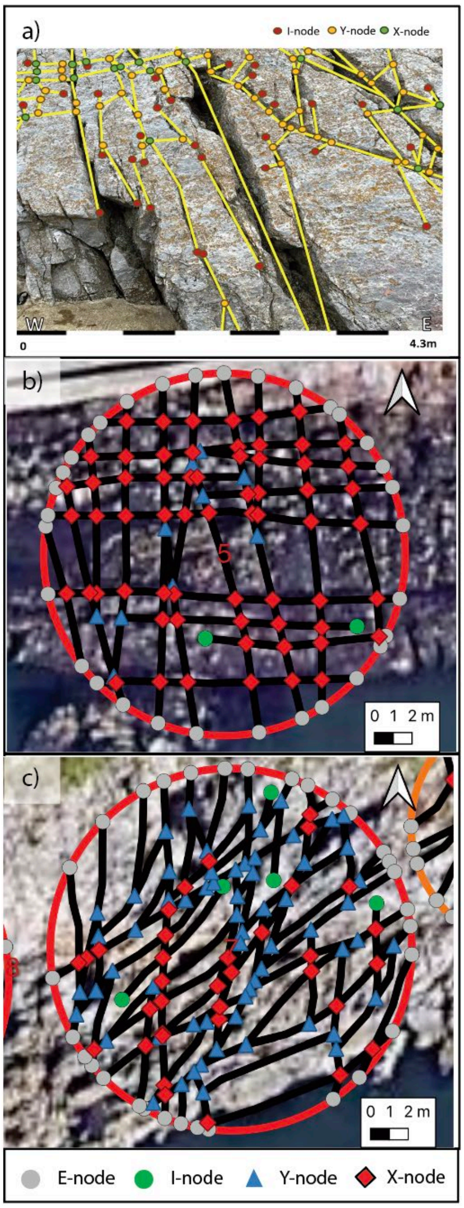

Figure 12 Interpreted topological sampling from a) FS 1 and representative sample circles b) 5 and c) 7.

Fracture orientation varied across the different scales of observation. Regional scale faults are strongly orientated NW-SE, with a subordinate ENE-WSW (Figure 10a). Between these primary trends, faults plot within the easterly and westerly quadrants of the rose diagram, with very few structures trending N-S (Figure 10). Within the study area, regional faults show similar orientations to the regional population, with longer faults trending NW-SE and shorter ENE-WSW faults commonly offset by the NW-SE set (Figure 10b). Where regional faults intersect the foreshore, they are typically obscured by coastal engineering (Figure 10b). However, 16 additional NW-SE trending features were identified from linear scanlines LS1-3. These features form large-aperture caves or gaps in the outcrop, ranging from 0.3 to 8.8 m in width (average 2.2 m), with spacings of 1.85 to 104.2 m (average = 26.5 m). These features are interpreted as subsidiary faults, although further analysis was not possible due to outcrop and access limitations.

Comparison of regional structures with fracture orientations from circular scanlines and field stations highlights significant differences in fracture orientation (Figure 10a-b, Figure 12, Figure 13). Circular scanline data shows a dominant N-S trend with limited dispersion, with a more disperse NE-SW set, and no fractures trending ESE-WNW (Figure 10bi). In some locations, these two fracture sets are mutually cross-cutting (Figure 12b), whereas in others the E-W to NW-SW set abuts against the more northerly trending set, suggesting a younger relative age (Figure 12b, c). Spatial variations in fracture orientation occur across the study area (Figure 10bii-vii). The N-S fracture set is consistently present, whereas the secondary set varies from NE –SW in the western (up to major fault 2; Figure 10bii, iii) and eastern areas (between major faults 6 and 7), to E–W to ENE–WSW in the centre of the study area (between major faults 4 and 6; Figure 10biv,v). The only area where fracture orientations closely resemble the regional fault pattern occurs between major faults 1 and 2 (Figure 10biii), where N–S, NE–SW, and subsidiary regional-scale trends are observed. Orientations extracted from aerial imagery correspond closely with those measured at field stations (Figure 13). Stereonet analysis shows dips range from 26˚to 86˚(average 63˚), and that the N–S fracture set comprises conjugate fractures at FS1 and FS2, whereas at FS2 it is represented by a single easterly dipping set. The ENE–WSW to NE–SW fracture set consistently displays conjugate relationships.

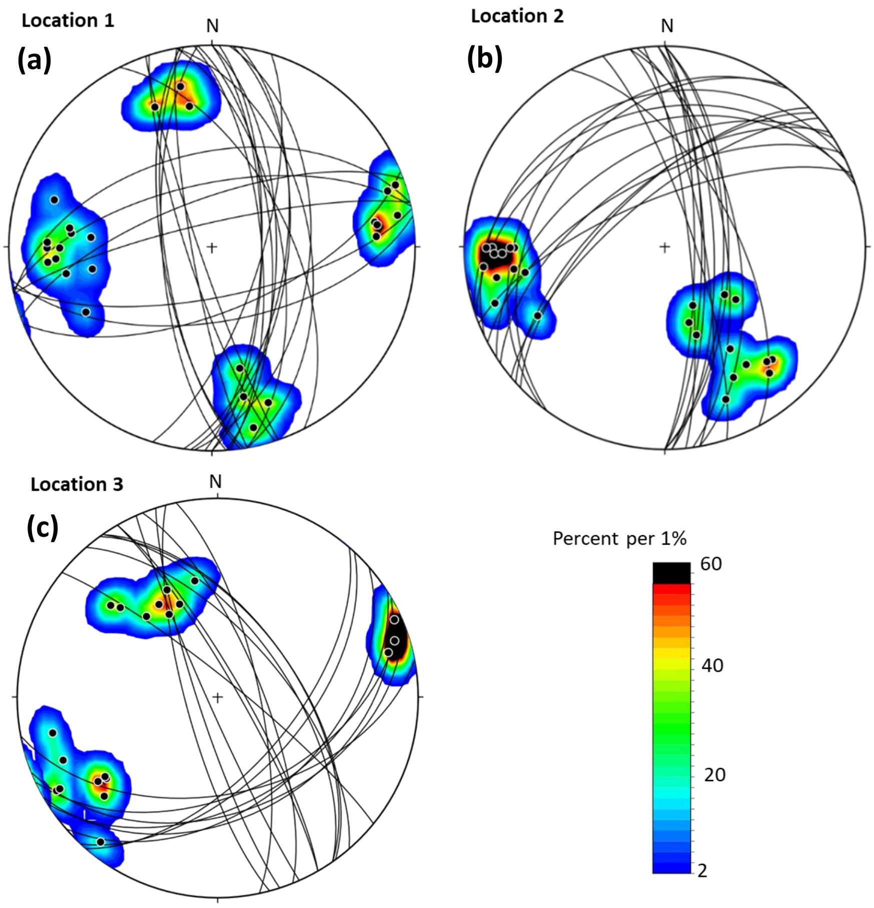

Figure 13 Stereographic projections for dip and dip-direction of fractures collected at a) FS1, b) FS2, and c) FS3 respectively. Stereonet 11 (Allmendinger, 2020) was used to plot and analyse the data. Note how across all field stations, the dip of fractures is high, with N-S to NNW-SSE and NE-SW trending fractures dominating, but that some of the orientation sets consist of conjugate fractures.

Fracture intensity across the Plymouth Limestone is high, with averages of 3.9 f/m from field stations and 0.8 f/m from circular scanlines (Supplementary SI-3). The difference between methods reflects the large number of short trace-length fractures observed at outcrop (Figure 11a). As circular scanlines capture the connected fracture network and provide consistent measurements across the full study area, these data are considered more representative of reservoir-scale fracture properties. Similar to fracture orientation, spatial variations in network properties are observed across the study area (Figure 10c-e). Fracture intensity ranges from 0.52 to 1.18 f/m, with low variability in the west, greater variability in the east, and generally lower values between major faults 4 and 6 (Figure 10c). Fracture density ranges from 0.02 to 0.29 f/m² (average = 0.12 f/m²) and follows similar spatial trends to fracture intensity. The consistently lower density relative to intensity indicates that fractures within the sampled network are relatively long, with few short fractures contained within the sample windows, further supporting the presence of a truncated fracture population and suggesting flow through the reservoir will be controlled by laterally extensive fractures.

The aperture of several faults and joints has been enhanced by karstic dissolution and weathering processes. Aperture measurements were only possible at the field stations (Supplementary SI-3), where 55% of fractures were closed, 9.5% were tight, 7% were infilled by limestone fragments, and 26% were open, occasionally containing pebble infill. Based on the classification scheme of Bieniawski (1989), mean apertures recorded across the scanlines ranged from close (60 to 200 mm; 60% of scanlines) to moderate (200 to 600 mm; 40% of scanlines) across the three field stations. These aperture measurements likely represent an upper estimate for the aquifer due to enhanced coastal weathering; however, apertures of ~200 mm is not unrealistic, and apertures >10 mm may persist at depth. Based on fracture spacing, and aperture estimates, fracture porosity within the coastal zone is estimated to range from 0.3 and 16.2%, with an average value of XX% (Supplementary X).

The connectivity and distribution of node types vary across the study area and between datasets (Figure 11, Figure 12). Across all datasets, the network is dominated by connected nodes, with relatively low proportions of I-nodes. The proportion of I-nodes is consistently higher in remotely sensed datasets compared with field photographs (Figure 12b). In field photographs, isolated nodes typically represent either short trace-length isolated fractures or small fractures that abut larger through-going fractures (Figure 12a). Due to their limited aperture and enhanced coastal weathering, these features are likely below the resolution of aerial imagery. Furthermore, their short trace lengths and isolated to partially isolated nature mean that they contribute little to overall network connectivity, although they may increase local porosity. Circular scanlines show significant variability in Y- and X-node proportions, with some sample circles dominated by X-nodes due to mutually cross-cutting long fractures extending beyond the sample boundary (Figure 12b), whereas others are dominated by Y-node relationships (Figure 12). No systematic spatial trend in node distributions is observed across the study area. Instead, variations appear to reflect local differences in fracture architecture, including the presence of small faults (e.g., the NNE–SSW lineament in Figure 12) that locally modify the balance between X- and Y-dominated networks. Despite variability in node proportions, fracture networks remain highly connected (Figure 10d). Connections per line range from 3.05 to 45.33 (average = 8.73), and connections per branch range from 1.72 to 2.00 (average = 1.93). These values are slightly higher than those calculated from field stations, which range from 1.47 to 3.21 and 1.25 to 1.73 for connections per line and connections per branch, respectively. Across both datasets, all circular scanlines and field stations FS1 and FS2 exceed the minimum structural percolation limit, while all locations except FS3 exceed the threshold for long-range connectivity. These results indicate that the Plymouth Limestone fracture network is sufficiently connected to support flow between major faults and, combined with the observed fracture properties, suggests that the aquifer is likely conductive even away from major fault zones (Table 4).

Table 4 Summary of fracture network properties and the implications for the Plymouth Aquifer.

Fracture property	Summary of results	Implications for the Plymouth Coastal Aquifer
Regional faults (Present on the BGS map)	Dominated by NW-SE trending structures, which crosscut subordinate earlier ENE-WSW faults. Major faults show enhanced karstification and are expressed as voids or covered by coastal engineering along the Plymouth foreshore.	Major faults provide the first order structural framework for groundwater flow and likely act as the principal high permeability conduits. Major faults also sub-divide the reservoir into blocks where fracture network properties within each block differ (as described below).
Fracture orientation	Fracture orientations differ from the regional fault pattern and vary between fault bound blocks, with persistent N-S to NNW-SSE and NE-SW to ENE-WSW fracture sets dominating. Cross cutting relationships suggest the N-S to NNW-SSE set occurred later.	The wide range of orientations present in the network supports a well-connected network which promotes groundwater flow in multiple directions, including away from the regional faults. Local orientation changes may locally alter the permeability structure of the reservoir and produce permeability anisotropy to develop.
Fracture length	Our data is highly truncated across all methods, however, the ability to fit a power law across all scales suggests the network is not scale dependent.	The length distribution of fractures within the Plymouth Limestone is at least in part predictable, suggesting our findings can be upscaled to the whole aquifer.
Fracture intensity & density	Fracture intensity is consistently high across the study area, although varies spatially with lower intensities between major faults 4 and 6. Density shows a similar trend, although is far lower, indicating that long fractures dominate the network.	High fracture intensity suggests pervasive fracture porosity exists throughout the Plymouth Limestone, allowing groundwater flow between major faults rather than flow being restricted to fault damage zones.
Fracture aperture	Approximately 25% of fractures remain open, with apertures ranging from close to moderate. Estimated fracture porosity ranges from 0.3 to 16.2%, although coastal weathering means this likely represents an upper bound.	Open fractures provide effective groundwater pathways and storage. Although apertures are likely reduced at depth, the shallow nature of the aquifer and presence of karstification along fractures means fractures are likely to be hydraulically significant throughout the aquifer.
Fracture connectivity	Fracture networks are dominated by Y- and X- nodes and consistently exceed published percolation thresholds. Connections per line and per branch both indicate system-spanning connectivity across almost the entire study area.	The fracture network can support long-range groundwater flow throughout the Plymouth Limestone, with permeability maintained even in areas away from major mapped faults.

5.2 Rock properties

Like the mineralogy of the Plymouth Limestone, the limestone found within the Torpoint Formation is greatly recrystallised (Leveridge et al.,2002), leading to the development of a sparry calcite mosaic and reduced original porosity. Calcite in thin section is easily identifiable by its rhombohedral cleavage and high-order interference colours, reflecting its strong birefringence (see Figure 14C).

Large calcite crystals occur throughout both formations, with some exhibiting evidence of deformation and stress, including lamellar twinning, bent cleavage, and undulose extinction (Figure 14A and B and F). Intergranular pore space is locally abundant in O-TF1-2, appearing black in XPL and colourless in PPL, possibly representing secondary porosity formed through later dissolution of the recrystallised matric. Furthermore, the larger calcite crystals are surrounded by a fine-grained calcitic matrix, producing a well-cemented fabric, see Figure 14E, G and H.

SEM images of the Torpoint Formation show notable textural variations in their microstructure. Figures 15A and B comprise a highly cemented fabric with varying grain angularities and sizes. The majority of grains are <2µm in size, although occasional larger rounded particles (~2.5µm) are present. Visible intergranular pore space occurs locally in Figure 15B, whereas Figure 15A exhibits less visible porosity with a smoother surface, possibly indicating a higher cemented matrix.

The percentage porosity of TF1 was calculated by measuring pore space area relative to total image area using ImageJ. The thresholding tool was applied via ImageJ, highlighting pore networks in red (Figure 15B), enabling quantitative assessment of pore geometry, connectivity, and spatial distribution. Multiple replicates of TF1 were analysed due to its wide variation in visible pore space. As presented in Table 5, ImageJ analysis demonstrated a low average primary porosity of 5.23%, with pore spaces appearing mostly isolated and indicated poor connectivity within the rock's crystallised matrix. This crystallisation leads to a dense and brittle rock more prone to fracturing, aiding the transport of fluids and dissolution. Although limestones can also vary massively, ranging from 0.1 – 40% porosity, with the higher end corresponding to soft white chalk, crystalline limestone generally ranges from 0.1 – 10% (Blatt *et al.* 1980) placing the TF1 average of 5.23% in the middle.

Furthermore, optical microscopy showed extensive recrystallisation of the Plymouth Limestone, reflected by the large sparry calcite crystals and surrounding well-cemented calcite groundmass. This diagenetic alteration has reduced primary pore space, consistent with porosity analysis measured from SEM imagery. Calcite veins in thin section also provides past evidence of groundwater movement within fractures as shown in Figure 14D. Both the Plymouth Limestone (BH-PL) and Torpoint Formation limestone (BH-TF) are greatly recrystallised and therefore share many similarities, including high-order birefringence colours and fine-grained calcitic matrix, figure 14C and E. Larger calcite crystals are abundant in both formations, many of which demonstrate bent cleavage and undulose extinction, which can be attributed to a similar diagenetic history. As a result of the sparry calcite cement, intergranular pore space is limited, reducing primary porosity.

This combined indicates that groundwater flow within the formation is not controlled by primary porosity due to limited matrix storage, but instead by secondary permeability including microfractures and karstic dissolution features. Saline intrusion therefore would be more likely to be restricted to fractures rather than the rock's matrix, supporting a low risk of irreversible salinisation of the aquifer.

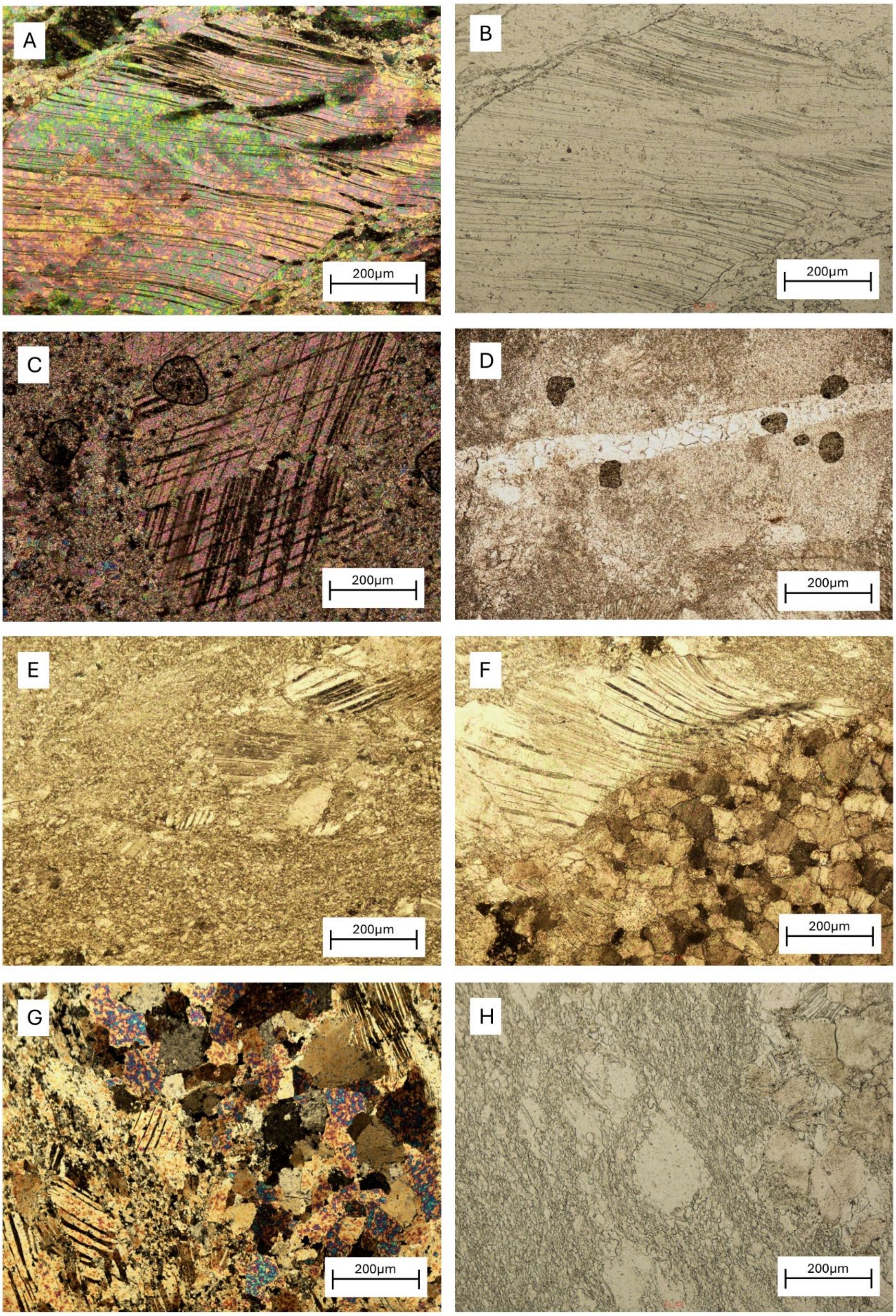

Figure 14 Thin section images identifying recrystallised matrix in TF1 and PL1; O-PL5 XPL (A), O-PL5 XPL (B), O-TF1 XPL (C), O-TF2 PPL (D), O-PL1 XPL (E), O-PL2 PPL (F), O-PL3 XPL (G), O-PL4 PPL (H).

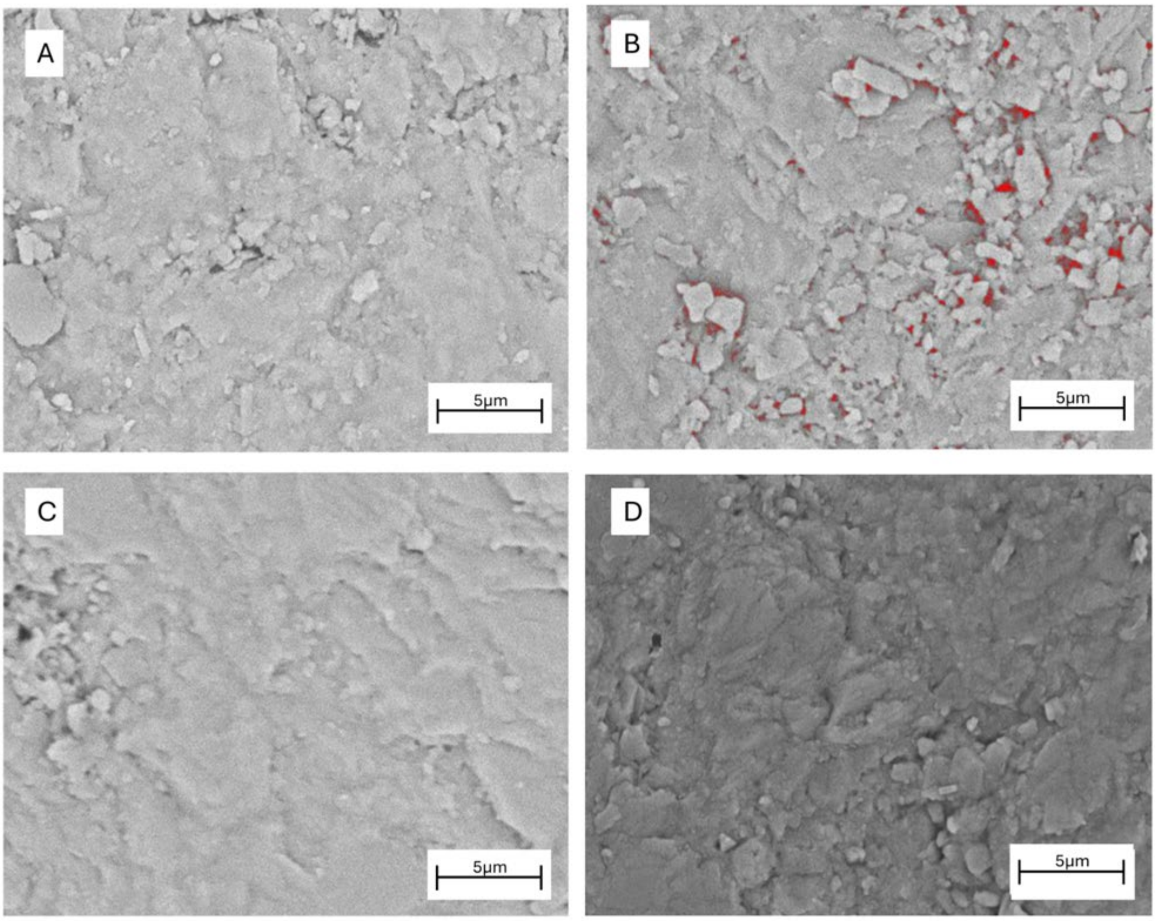

Figure 15 x5000 magnification SEM images S-TF1 (A - D). Top right image (B) highlights pore space in red as seen in ImageJ.

Table 5 Summary of porosity data of Torpoint Formation, as determined by ImageJ

Image N.	% area
S-TF1a	6.214
S-TF1b	6.443
S-TF1c	3.333
S-TF1d	7.004
S-TF1e	4.091
S-TF1f	3.19
S-TF1g	8.295
S-TF1h	4.245
S-TF1i	4.733
S-TF1j	3.581
S-TF1k	6.31
S-TF1l	4.24
S-TF1m	4.219
S-TF1n	6.475
S-TF1o	11.878
S-TF1p	5.432
S-TF1q	4.4
S-TF1r	4.916
S-TF1s	3.714
S-TF1t	1.855
Av %area	**5.2284**

These results agree well with those from analyses undertaken in the 'Massenkalk' Limestones, with common fracture porosity present that have a total range of 2.84% to 7.52%, together with low permeabilities measured along those fractures of 2.28×10^{-18} m^2 to 1.11×10^{-16} m^2 (Lippert *et al.* 2022). However, where the 'Massenkalk' Limestones are karstified, effective porosities increase up to 14.24%, and where they are dolostones, porosities are 4.65% (Heinelt *et al.* 2026).

5.3 Hydrogeochemistry

Limited complete hydrogeochemical data are available for the Plymouth Aquifer, here we present measurements reported by Roxburgh (1983) and new data from the 2022 and 2023 pumping test (Table 6). Additionally, data for the Plymouth Gin Distillery well are presented, the sample was taken from the cistern following a three-day phase of clearance pumping.

Historical monitoring data from Roxburgh (1983) is indicative of low salinity, meteoric waters with moderately high hardness (calculated as 85 – 190 mgl^{-1} as $CaCO_3$ equivalents from Ca and Mg ions, noting potentially erroneous readings with published data). Saltram and Pomphlett Quarries are located to the East of Plymouth City Centre, across the River Plym and are whilst within the Plymouth Limestone, they are hydraulically independent from the Plymouth Aquifer beneath the city. The Regents Brewery, Stonehouse is located on a faulted boundary between the Saltash Formation (Slate and Siltstone) and the Plymouth Limestone, and Prysten House, Barbican also within the city is located in the Plymouth Limestone. Chloride concentrations of <100 mgl^{-1} are indicative of minimal saline intrusion in these locations, suggesting fresh water flowing coastward remained at this time. This is in contrast to salinisation of wells reported between these two locations (Victoria Spa and Octagon Brewery) more than a century before (Ussher 1907; Roxburgh 1983). The depth of the intake and pumping regime are unknown for these data.

Blackfriars' Well at Plymouth Gin Distillery is located approximately 150m West from the coast at its closest proximity (Guy's Quay, Sutton Harbour) and approximately 450m North from the seaward foreshore where the limestone outcrops (Figure 2). During *recent sampling (*2022; 2025) the Blackfriars Well was poorly mineralised with a low salinity (Cl <100 mgl^{-1}), though it was noted that water was abstracted from a shallow depth in this location (intake <7mbgl). Clearance pumping of ~100m^3 was undertaken prior to the 2024 sample (Lawson 2025), this sample yielded moderately high alkalinity (146 mgl^{-1} as $CaCO_3$) indicative of water-rock interaction with carbonate minerals. Buckwell borehole, a short distance inland, was also characteristic of this low salinity facies when grab-sampled in 2022. Whilst there is historical evidence that the aquifer was degraded at depth, shallow private wells close to the coast were still utilized into the 20th century and today still yield groundwater of low salinity, raising the possibility of a stratified halocline within the aquifer.

Plymouth Pavillions Borehole (BDH, cased to 82mbgl) became saline rapidly after pumping commenced, however a significant freshwater component was observed in both tests, with maximum measured chloride of 15,100 mgl^{-1} on the 6 July 2022 (seawater typically 19,000 mgl^{-1}). A grab sample immediately before the 2023 pumping test was alkaline (pH 8.9) and fresh (Cl 6 mgl^{-1}) which is indicative of rainfall interacting with constructional grout. Proximal boreholes BH1, BH3 and Harbour Car Park are of moderate salinity: 461 mgl^{-1}. 915 mgl^{-1} and 11,000 mgl^{-1} respectively, indicative of residual seawater mixing within this region.

Excepting one sample from the Blackfriars Well, iron concentrations remained exceptionally low (≥0.01mgl^{-1}), meaning the risk from groundwater derived iron oxyhydroxide fouling is low. As reported in Section 3, the main water quality issue relates to significant quantities of entrained sediment from pumping of BHD.

Table 6. Hydrochemistry measurements, data presented as dissolved species unless otherwise reported.

Sample	pH	Hardness (mgl^{-1} as CaCO3)	Alkalinity (mgl^{-1} as CaCO3)	SO4 (mgl^{-1})	Cl (mgl^{-1})	NO3 (mgl^{-1})	Ca (mgl^{-1})	Mg (mgl^{-1})	Na (mgl^{-1})	K (mgl^{-1})	Fe (mgl^{-1})		Mn (mgl^{-1})
											Total	0.45 µm Filtered	
Regents Brewery, Stonehouse (SX 4635 5435), Roxburgh 1983	7.60	475.8#	-	74.0	56.0	9.1	26.67	5.46	8.3	1.0	-	-	-
Prysten House, Barbican (SX 4792 5437), Roxburgh 1983	7.60	436.6#	-	74.0	39.8	9.1	31.9	3.7	7.4	1.9			-
Pomphlett Quarry (SX 5088 5386), Roxburgh 1983	7.54	433.1#	-	59.7	33.0	10.7	60.9	7.77	9.6	1.2	-	-	-
Saltram Quarry (SX 5082 5435), Roxburgh 1983	7.73	518.6#	-	88.3	24.8	13.5	60.9	10.7	0.9	0.4	-	-	-
Blackfriars' Well*, Lawson 2025	-	-	146	10.9	51.7		40.52	4.79	27.8	7.2	1.88	1.17	0.61
Blackfriars' Well* (2022)	7.6	89.7	-	30	71	1.2	31	3	43	6	-	0.01	0.002
BH03* (2022)	8.1	337	-	267	915	1.2	42	56	564	58	-	0.01	0.975
15/47/002/G/044 (Aquarium, 2022)*	8	5540	-	2420	10100	1.5	236	1140	8810	573	-	<0.01	<0.002
BH01 (2022)*		462	-	277	461	1.3	116	42	390	38	-	0.01	0.006
Buckwell (2022)*	7.6	165	-	55	44	16.2	58	5	37	23	-	0.01	<0.002
Harbour Car Park (2022)*	7.6	3910	-	1180	11000	<0.2	193	766	5340	345	-	0.01	0.451
BHD* (1/07/2022)	7.3	3790	-	1590	9760	<0.2	253	693	5530	332	-	0.01	1.04
BHD* (4/07/2022)	7.4	5390	-	2330	10600	<0.2	268	992	8110	490	-	<0.01	0.464
BHD* (6/07/2022)	7.3	4950	-	2030	15100	1.5	356	916	7860	460	-	<0.01	0.458
BHD* (6/07/2022)	7.3	4680	-	1910	13800	0.4	342	867	7240	425	-	<0.01	1.15
BHD* (5/06/2023)	7.2	4530	171	1820	14000	0.6	240	847	6890	415	-	<0.01	0.12
BHD* (5/06/2023)	8.9	27.4	-	<3	6	<0.2	8	2	5	<1	-	<0.01	<0.002
Pavilions Borehole (BHD*), Adibeli 2024	-	-	-	2197.0	12663.0	-	415	875	7895.0	460	-	-	-

*See Figure 2. for sampling locations; # values from literature thought to be erroneous

5.4 Resource assessment model for Plymouth

The fracture network within the Plymouth Aquifer exhibits distinct geometric characteristics across the study area. The close-moderate fracture intensity observed from field data suggests a moderately jointed rock mass where fractures accommodate significant regional strain (Gholipour *et al.* 2016). Orientation analysis reveals a complex stress history, displaying roughly orthogonal cross-joint systems, implying a ~90° rotation in regional stress directions during formation (Bai *et al.* 2002). Importantly, such orthogonal fracture geometry and high density of NNW-SSE trending fractures at the three field locations implies both good fracture interconnectivity and, good connection with the coastal fringe (immediately to the south of the city). These findings are in agreement with larger-scale mapped faults which transect the Devonian limestone aquifer and persist well into the siltstones and slates to the north. Porosity calculations reveal the dual nature of this system. Surface aperture measurements yield inflated porosity percentages (up to 26% at field location 1) due to weathering and karstic widening at the outcrop. When adjusted for hydraulic apertures based on deep-fracture distributions from Spasojević (2025), fracture porosity drops significantly (~0.02-0.03%). However, this low value likely fails to account for the extensive karstification found in the Plymouth Aquifer, which is likely to follow structural planes of weakness trending NNW, SSE.

The interplay between the structural model and karst processes defines the hydrogeology of the Plymouth Aquifer. The structural dip and thrust boundaries have created a "B-type" aquifer where the base level of erosion is lower than potential allogenic inputs, facilitating rapid groundwater response to recharge (Easterbrook and Smith, 2018). The observed fractures serve as primary conduits but are certainly amplified by weathering. Large voids and tube-like openings found at location 1 & 2, show that dissolution has widened surface fractures into significant flow paths, increasing the conductivity of the reservoir, both from natural inland recharge and, in reverse, during abstraction, drawing in seawater from the coast. The karst processes driven by the coastal setting of the aquifer and long-term sea-level fluctuations (Easterbrook and Smith, 2018) have enhanced the connectivity and storage potential of the Plymouth Aquifer.

Uknown potential exists for deeper connections to geothermal anomalies at depth associated with granite intrusions in the vicinity. The deepest boreholes in Plymouth available on the public record extend no more than a few hundred metres below ground level. This means significant geological uncertainty at depth beneath the known Plymouth Aquifer, though significant structural features have been mapped which could provide conduits for geothermal waters. Further data needs to be acquired to evaluate the geothermal resource, which could comprise (in sequence of increasing cost) geochemical tracer (natural and anthropogenic) analysis of coastal springs; geophysical investigations such as seismic surveys and, drilling of a deep exploratory well.

6. Conclusions

Coastal aquifer energy is explored for the city of Plymouth, UK, where coastal abstractions have shown good connectivity with the sea via a karstified limestone aquifer system. It is hypothesized that extraction of sea water via wells on the coastal fringe represents a cost effective and sustainable approach to accessing an ambient thermal resource for district heating and cooling applications.

In Plymouth, karstic features, periglacial deposits, and/or modern channel infill material, presented challenges of sediment influx into a high-yielding borehole. However, data from boreholes in other locations in the city's coastal region suggests that this may not be a pervasive issue.

Structural data from field surveys and aerial imagery indicate persistent fractures within the sampled network, suggesting that flow through the reservoir is likely to be controlled by laterally extensive fractures. Fracture network analysis identifies y and x nodes dominate and strong NNE, SSW strike pattern matching BGS mapped faults, hydraulically interconnecting major structures and providing connectivity with the sea. Furthermore, karstification identifiable by macro-scale coastal scanlines, exhibits 0.32 – 9.5% void space along the coastal fringe, indicative of a cave network likely persisting along major NNE, SSW trending faults.

Microstructural data for rock cores indicates the limestone has undergone extensive recrystallisation leading to a low pore connectivity and an average primary porosity of 5.23%, likely due to burial history and low grade metamorphism of the sediments. This confirms that the aquifer porosity is fracture-dominated (secondary porosity) and that any saline intrusion via coastal abstractions is likely to be reversible.

Pumping test water quality analysis demonstrates strong connection with the marine environment, with water rapidly turning ~1/3 saline yet retaining a freshwater component. Limited hydrochemistry data from grab samples at monitoring wells suggests a freshwater gradient from the North, likely migrating into the limestone aquifer via structural features within otherwise low permeability indurated siltstones and slates from areas of recharge north of the city, potentially in a stratified manner presenting as a halocline. Such structural features may also provide conduits for the flow of deeper, true geothermal waters linked to granite plutons within the region.

Further work is required to better de-risk aquifer energy in Plymouth, specifically relating to potential sources of suspended sediment in pumped wells, flow paths within the coastal fringe aquifer and influence zones with the adjacent buried channel alluvial deposits. Desk study information and existing knowledge of effective abstractions by Plymouth Marine Aquarium could be used effectively in this effort, with the potential for developing a monitored demonstrator project in this part of the city. Additionally, application of groundwater tracers would confirm hydrogeological flow paths for shallow aquifer energy and provide valuable insights into the potential for deeper geothermal resources within the city boundary.

7. Acknowledgements

Justin Etherington, Director, Buro Happold Engineering is acknowledged for identifying the potential for aquifer thermal energy storage in the first instance and constructive engagement following the 2022 and 2023 testing campaigns. The authors would like to thank colleagues from the University of Plymouth for technical support: Jess Berry for preparation of thin sections, Marc Davies and Kat Piper for assistance with microscopy. Jamie Quinn is credited with image production. The authors would also like to thank Gary Holmes, W.J. Groundwater Ltd., who was involved in the planning and oversaw the contractor activities during the 2022 and 2023 test campaigns. Robin Lawrence, Industrial Water Specialist, Worley Consulting Ltd, for internal review of Worley Consulting Ltd contribution to this article. Brian Lewarne, Devon Karst Research Society for helpful steer through the project and provision of information and insights on the karst aquifer system.

8. Author contributions

MTB led the development of the manuscript, framing and writing synthesis, and was supervisor for final year research projects undertaken by EL and OF. DB developed the coastal discharge aquifer energy concept in Plymouth and led the development history and learning section. RPS developed the initial conceptual model presented herein and contributed local expertise on the aquifer system. JS championed the aquifer energy project and contributed to the introductory material relating to the heat networks. OF collected structural field data and co-led the structural data section. EL collected the microstructural laboratory imagery and led the microstructural section. NH led the geological background section. BA led the structural analysis and undertook remote sensing structural surveys.

9. References

Alexander, A. and Shail, R. 1996. Late-to post-Variscan structures on the coast between Penzance and Pentewan, south Cornwall. *Proceedings of the Ussher Society*, **9**, 72-78.

Ali, H., Hlebnikov, A., Pakere, I. and Volkova, A. 2024. An evaluation and innovative coupling of seawater heat pumps in district heating networks. *Energy*, **312**, 133461, https://doi.org/https://doi.org/10.1016/j.energy.2024.133461.

Andrews, B.J., Roberts, J.J., Shipton, Z.K., Bigi, S., Tartarello, M.C. and Johnson, G. 2019. How do we see fractures? Quantifying subjective bias in fracture data collection. *Solid Earth*, **10**, 487-516, https://doi.org/10.5194/se-10-487-2019.

Bai, T., Maerten, L., Gross, M.R. and Aydin, A. 2002. Orthogonal cross joints: do they imply a regional stress rotation? *Journal of Structural Geology*, **24**, 77-88, https://doi.org/https://doi.org/10.1016/S0191-8141(01)00050-5.

Bailey, M.T., Gandy, C.J., Watson, I.A., Wyatt, L.M. and Jarvis, A.P. 2016. Heat recovery potential of mine water treatment systems in Great Britain. *International Journal of Coal Geology*, **164**, 77-84, https://doi.org/https://doi.org/10.1016/j.coal.2016.03.007.

Balberg, I., Anderson, C.H., Alexander, S. and Wagner, N. 1984. Excluded volume and its relation to the onset of percolation. *Physical Review B*, **30**, 3933-3943, https://doi.org/10.1103/PhysRevB.30.3933.

Banks, D., Steven, J., Black, A. and Naismith, J. 2022. Conceptual Modelling of Two Large-Scale Mine Water Geothermal Energy Schemes: Felling, Gateshead, UK. *International Journal of Environmental Research and Public Health*, **19**, 1643.

Bieniawski, Z.T. 1989. *Engineering rock mass classifications: a complete manual for engineers and geologists in mining, civil, and petroleum engineering*. John Wiley & Sons.

Billerbeck, A., Kiefer, C.P. *et al.* 2024. The race between hydrogen and heat pumps for space and water heating: A model-based scenario analysis. *Energy Conversion and Management*, **299**, 117850, https://doi.org/https://doi.org/10.1016/j.enconman.2023.117850.

Birks, D. 2023. Mine water geothermal – what might a viable business case look like. *UK Mine Water Energy Symposium*, Online, 19-20 April 2023.

Birks, D., Adamson, C., Woods, M.G. and Holmes, G. 2022. Evaluation of measures to improve the performance of an open loop ground source heat pump system in the chalk aquifer: a case study. *Quarterly Journal of Engineering Geology and Hydrogeology*, **55**, 21-74, https://doi.org/doi:10.1144/qjegh2021-074.

Birks, D.C. 2019. *Groundwater heating and cooling-an evaluation of resilience in the context of recharge and temperature.* PhD, University of Glasgow.

Blatt, H., Middleton, G. and Murray, R. 1980. *Origin of sedimentary rocks*. 2 ed. Prentice-Hall.

Bluck, B.J., Cope, J.C.W. and Scrutton, C.T. 1992. Devonian. *Geological Society, London, Memoirs*, **13**, 57-66, https://doi.org/doi:10.1144/GSL.MEM.1992.013.01.08.

Braithwaite, C.J.R. 1967. Carbonate environments in the middle devonian of South Devon, England. *Sedimentary Geology*, **1**, 283-320, https://doi.org/https://doi.org/10.1016/0037-0738(67)90065-6.

Brooks, M., Doody, J.J. and Al-Rawi, F.R.J. 1984. Major crustal reflectors beneath SW England. *Journal of the Geological Society*, **141**, 97-103, https://doi.org/10.1144/gsjgs.141.1.0097.

Cefas 2026. Sea temperature and salinity trends, Station 25, Plymouth.

Chapman, T., Fry, R. and Heavey, P. 1984. A structural cross-section through SW Devon. *Geological Society, London, Special Publications*, **14**, 113-118.

Chinello, M., Bordignon, S., Marigo, M., Pockelé, L., Di Bella, A. and De Carli, M. 2026. Assessment of cooling demand for buildings in Europe. *Energy and Buildings*, **361**, 117440, https://doi.org/https://doi.org/10.1016/j.enbuild.2026.117440.

Cotton, L., Gutmanis, J., Shail, R., Dalby, C., Batchelor, A., Foxford, A. and Rollinson, G. 2020. Geological Overview of the United Downs Deep Geothermal Power Project, Cornwall, UK. *Proceedings of the World Geothermal Congress, Reykjavik, Iceland*, 24-27.

Coward, M.P. and McClay, K.R. 1983. Thrust tectonics of S Devon. *Journal of the Geological Society*, **140**, 215-228, https://doi.org/10.1144/gsjgs.140.2.0215.

Coward, M.P. and Smallwood, S. 1984. An interpretation of the Variscan tectonics of SW Britain. *Geological Society, London, Special Publications*, **14**, 89-102, https://doi.org/doi:10.1144/GSL.SP.1984.014.01.08.

Cross, N.E. and Burchette, T.P. 2025. Middle Eastern carbonate reservoirs – the critical impact of discrete zones of elevated permeability on reservoir performance. *In*: Garland, J., Barnett, A.J., Burchette, T.P. and Wright, V.P. (eds) *Carbonate Reservoirs: Applying Current Knowledge to Future Energy Needs*. Geological Society of London, 0, https://doi.org/10.1144/sp548-2023-144.

Custodio, E. 2010. Coastal aquifers of Europe: an overview. *Hydrogeology Journal*, **18**, 269-280, https://doi.org/10.1007/s10040-009-0496-1.

Dearman, W.R. 1963. Wrench-faulting in Cornwall and south Devon. *Proceedings of the Geologists' Association*, **74**, 265-287, https://doi.org/https://doi.org/10.1016/S0016-7878(63)80023-1.

Dodson, M.H. and Rex, D.C. 1970. Potassium–argon ages of slates and phyllites from south-west England. *Quarterly Journal of the Geological Society of London*, **126**, 465-498, https://doi.org/doi:10.1144/gsjgs.126.1.0465.

Easterbrook, C. and Smith, R. 2018. 'Evidence' for transition between Authigenic and Allogenic Aquifer functioning related to Regional Uplift and Sea Level Change in the Plymouth Coastal Karst Aquifer. *Proceedings of the Ussher Society*, **14**, 198–206, https://doi.org/http://ussher.org.uk/wp-content/uploads/journal/2017/Smith-198-206.pdf.

Farndale, H., Law, R. and Beyon, S. 2022. An Update on the United Downs Geothermal Power Project, Cornwall, UK. *Conference Proceedings, 47th Workshop on Geothermal Reservoir Engineering Stanford University, Stanford, California.* Workshop on Geothermal Reservoir Engineering.

Gao, L., Naylor, P., Hegab, A. and Pilidis, P. 2026. 'Greening' the UK: A Comparative Study of Heat Pumps and Hydrogen Boilers in Residential Heating. *Energies*, **19**, 156, https://doi.org/https://doi.org/10.3390/en19010156.

Garland, J. 1997. *Middle to Upper Devonian (Givetian and Frasnian) shallow-water carbonates of Western Europe: facies analysis and cyclicity.* PhD, Durham University.

Gayer, R. and Nemcok, M. 1994. Transpressionally driven rotation in the external Variscides of south-west Britain. *Proceedings of the Ussher Society*, **8**, 317-317.

Gholipour, A.M., Cosgrove, J.W. and Ala, M. 2016. New theoretical model for predicting and modelling fractures in folded fractured reservoirs. *Petroleum Geoscience*, **22**, 257-280, https://doi.org/doi:10.1144/petgeo2013-055.

Gille, D. 2003. Seawater intakes for desalination plants. *Desalination*, **156**, 249-256, https://doi.org/https://doi.org/10.1016/S0011-9164(03)00347-3.

Golonka, J. 2020. Late Devonian paleogeography in the framework of global plate tectonics. *Global and Planetary Change*, **186**, 103129, https://doi.org/https://doi.org/10.1016/j.gloplacha.2020.103129.

Hamblin, R., Crosby, A., Balson, P., Jones, S., Chadwick, R., Penn, I. and Arthur, M. 1992. The Geology of the English Channel. United Kingdom Offshore Regional Report. *British Geological Survey. HMSO, London*.

Happold, B. 2019. *Specification for Plymouth City Centre District Heating Wells.* For Plymouth City Council.

Happold, B. and Council, P.C. 2025. Plymouth Heat Network Zoning, Zone Opportunity Report. *In*: DESNZ (ed.).

Harper, N.P.J. 2013. *Assessing the mechanical state of sediment and rock during deformation: the example of the Bude Formation, South-west England.* PhD, University of Leeds.

Harrison, J., Walls, D.B. and Burnside, N.M. 2026. Hydrogeological assessment of megawatt-scale low-carbon heat generation from a single mine water surface discharge. *Quarterly Journal of Engineering Geology and Hydrogeology*, **0**, qjegh2025-2158, https://doi.org/doi:10.1144/qjegh2025-158.

Hartley, A. and Warr, L. 1990. Upper Carboniferous foreland basin evolution in SW Britain. *Proceedings of the Ussher Society*, **7**, 212-216.

Heinelt, M., Mueller, M., Ahrens, B., Nehler, M., Alms, K. and Immenhauser, A. 2026. Geothermal potential of karstified Devonian carbonates in NW Germany. *Geothermics*, **136**, 103552, https://doi.org/https://doi.org/10.1016/j.geothermics.2025.103552.

Heydarizad, M., Pumijumnong, N., Mansourian, D., Anbaran, E.D. and Minaei, M. 2023. The deterioration of groundwater quality by seawater intrusion in the Chao Phraya River Basin, Thailand. *Environmental Monitoring and Assessment*, **195**, 424, https://doi.org/10.1007/s10661-023-11023-0.

Holder, M.T. and Leveridge, B.E. 1986. A model for the tectonic evolution of south Cornwall. *Journal of the Geological Society*, **143**, 125-134, https://doi.org/10.1144/gsjgs.143.1.0125.

Holdich, R.G. and Sinclair, I. 1992. Measurement of slurry solids content by electrical conductivity. *Powder Technology*, **72**, 77-87, https://doi.org/https://doi.org/10.1016/S0032-5910(92)85024-P.

Holdsworth, R.E. 1989. Short Paper: The Start-Perranporth line: a Devonian terrane boundary in the Variscan orogen of SW England? *Journal of the Geological Society*, **146**, 419-421, https://doi.org/10.1144/gsjgs.146.3.0419.

IEA 2023. Greenhouse Gas Emissions from Energy Data, https://www.iea.org/data-and-statistics/data-tools/greenhouse-gas-emissions-from-energy-data-explorer.

Klassen, J. and Allen, D.M. 2017. Assessing the risk of saltwater intrusion in coastal aquifers. *Journal of Hydrology*, **551**, 730-745, https://doi.org/https://doi.org/10.1016/j.jhydrol.2017.02.044.

Law, R., Cotton, L. and Ledingham, P. 2019. The united downs deep geothermal power project. *Conference proceedings, EGC 2019*.

Lawson, M. 2025. *Unpublished dataset collected as part of MSc research*. University of Plymouth

Leveridge, B., Holder, A., Goode, A., Scrivener, R., Jones, N. and Merriman, R. 2002. Geology of the Plymouth and South-east Cornwall area: Memoir for 1: 50,000 Geological Sheet 348. *British Geological Survey, London*.

Leveridge, B.E. and Hartley, A.J. 2006. The Variscan Orogeny: the development and deformation of Devonian/Carboniferous basins in SW England and South Wales. *In*: Brenchley, P.J. and Rawson, P.F. (eds) *The Geology of England and Wales*. Geological Society of London, 0, https://doi.org/10.1144/goewp.10.

Leveridge, B.E., Holder, M.T. and Day, G.A. 1984. Thrust nappe tectonics in the Devonian of south Cornwall and the western English Channel. *Geological Society, London, Special Publications*, **14**, 103-112, https://doi.org/doi:10.1144/GSL.SP.1984.014.01.09.

Lippert, K., Ahrens, B., Nehler, M., Balcewicz, M., Mueller, M., Bracke, R. and Immenhauser, A. 2022. Geothermal reservoir characterisation of Devonian carbonates in North Rhine-Westphalia (W. Germany): Mineralogy- and depofacies-related extrapolation of petrophysical parameters. *Geothermics*, **106**, 102549, https://doi.org/https://doi.org/10.1016/j.geothermics.2022.102549.

Manzocchi, T. 2002. The connectivity of two-dimensional networks of spatially correlated fractures. *Water Resources Research*, **38**, 1-1-1-20, https://doi.org/https://doi.org/10.1029/2000WR000180.

Mastrucci, A., van Ruijven, B., Byers, E., Poblete-Cazenave, M. and Pachauri, S. 2021. Global scenarios of residential heating and cooling energy demand and CO2 emissions. *Climatic Change*, **168**, 14, https://doi.org/10.1007/s10584-021-03229-3.

Mauldon, M., Dunne, W.M. and Rohrbaugh, M.B. 2001. Circular scanlines and circular windows: new tools for characterizing the geometry of fracture traces. *Journal of Structural Geology*, **23**, 247-258, https://doi.org/https://doi.org/10.1016/S0191-8141(00)00094-8.

McMahon, N.A. and Turner, J. 1998. The documentation of a latest Jurassic-earliest Cretaceous uplift throughout southern England and adjacent offshore areas. *Geological Society, London, Special Publications*, **133**, 215-240, https://doi.org/doi:10.1144/GSL.SP.1998.133.01.10.

Nixon, C.W., Sanderson, D.J. and Bull, J.M. 2011. Deformation within a strike-slip fault network at Westward Ho!, Devon U.K.: Domino vs conjugate faulting. *Journal of Structural Geology*, **33**, 833-843, https://doi.org/https://doi.org/10.1016/j.jsg.2011.03.009.

Nkonge, N. 2017. *Plymouth City-Wide District Energy Strategy.* Buro Happold Engineering for Plymouth City Council.

Nlend, B., Celle-Jeanton, H., Huneau, F., Ketchemen-Tandia, B., Fantong, W.Y., Boum-Nkot, S.N. and Etame, J. 2018. The impact of urban development on aquifers in large coastal cities of West Africa: Present status and future challenges. *Land Use Policy*, **75**, 352-363, https://doi.org/https://doi.org/10.1016/j.landusepol.2018.03.007.

ONS 2022. How the population changed in Plymouth: Census 2021, https://www.ons.gov.uk/visualisations/censuspopulationchange/E06000026/ [13 July 2026].

Ouarani, M., Bahir, M., Mulla, D.J., Ouazar, D., Chehbouni, A. and Dhiba, D. 2021. Groundwater quality deterioration and recharge modes in a semi-arid coastal aquifer: Essaouira Aquifer case study (Morocco). *Arabian Journal of Geosciences*, **14**, 1989, https://doi.org/10.1007/s12517-021-08267-w.

Peacock, D.C.P., Anderson, M.W., Morris, A. and Randall, D. 1998. Evidence for the importance of small faults on block rotation. *Tectonophysics*, **299**, 1-13, https://doi.org/https://doi.org/10.1016/S0040-1951(98)00195-4.

Procter, A. and Sanderson, D.J. 2018. Spatial and layer-controlled variability in fracture networks. *Journal of Structural Geology*, **108**, 52-65, https://doi.org/https://doi.org/10.1016/j.jsg.2017.07.008.

Rohrbaugh, M.B., Jr., Dunne, W.M. and Mauldon, M. 2002. Estimating Fracture Trace Intensity, Density, and Mean Length Using Circular Scan Lines and Windows. *AAPG Bulletin*, **86**, 2089-2104, https://doi.org/10.1306/61eede0e-173e-11d7-8645000102c1865d.

Rosenow, J. 2022. Is heating homes with hydrogen all but a pipe dream? An evidence review. *Joule*, **6**, 2225-2228, https://doi.org/10.1016/j.joule.2022.08.015.

Roxburgh, I. 1983. Notes on the hydrogeology of the Plymouth Limestone. *Proceedings of the Ussher Society*, **5**, 479-481.

Roxburgh, I.S. 1985. Thermal infrared detection of submarine springs associated with the Plymouth Limestone. *Hydrological Sciences Journal*, **30**, 185-196, https://doi.org/10.1080/02626668509490983.

Sanderson, D.J. 1979. The transition from upright to recumbent folding in the Variscan fold belt of southwest England: a model based on the kinematics of simple shear. *Journal of Structural Geology*, **1**, 171-180, https://doi.org/https://doi.org/10.1016/0191-8141(79)90037-3.

Sanderson, D.J. and Nixon, C.W. 2015. The use of topology in fracture network characterization. *Journal of Structural Geology*, **72**, 55-66, https://doi.org/https://doi.org/10.1016/j.jsg.2015.01.005.

Sanderson, D.J. and Nixon, C.W. 2018. Topology, connectivity and percolation in fracture networks. *Journal of Structural Geology*, **115**, 167-177, https://doi.org/https://doi.org/10.1016/j.jsg.2018.07.011.

Shail, R.K. and Alexander, A.C. 1997. Late Carboniferous to Triassic reactivation of Variscan basement in the western English Channel: evidence from onshore exposures in south Cornwall. *Journal of the Geological Society*, **154**, 163, https://doi.org/https://doi.org/10.1144/gsjgs.154.1.0163.

Shail, R.K. and Leveridge, B.E. 2009. The Rhenohercynian passive margin of SW England: Development, inversion and extensional reactivation. *Comptes Rendus. Géoscience*, **341**, 140-155.

Sills, G. 1998. Development of structure in sedimenting soils. *Philosophical Transactions of the Royal Society of London, Series A: Physical and Engineering Sciences*, **356**, 2515-2534, https://doi.org/10.1098/rsta.1998.0284.

Spasojević, S. 2025. Investigation of the Hydraulic Conductivity of Fractures in a Limestone Rock Mass. *OPEN JOURNAL OF MODERN HYDROLOGY Учредители: Scientific Research Publishing, Inc.*, **15**, 91-108.

Terzaghi, R.D. 1965. Sources of Error in Joint Surveys. *Géotechnique*, **15**, 287-304, https://doi.org/10.1680/geot.1965.15.3.287.

Ussher, W.A.E. 1907. *The Geology of the Country Around Plymouth & Liskeard*. HM Stationery Office.

Warr, L. 1995. A reconnaissance study of very low-grade metamorphism in south Devon. *PROCEEDINGS-USSHER SOCIETY*, **8**, 405-405.

Warr, L.N., Primmer, T.J. and Robinson, D. 1991. Variscan very low-grade metamorphism in southwest England: a diastathermal and thrust-related origin. *Journal of Metamorphic Geology*, **9**, 751-764, https://doi.org/https://doi.org/10.1111/j.1525-1314.1991.tb00563.x.

Watkins, H., Bond, C.E., Healy, D. and Butler, R.W.H. 2015. Appraisal of fracture sampling methods and a new workflow to characterise heterogeneous fracture networks at outcrop. *Journal of Structural Geology*, **72**, 67-82, https://doi.org/https://doi.org/10.1016/j.jsg.2015.02.001.

WJGL 2022. *Pumping Test Factual Report, Bath Street, Plymouth*. . *Unpublished report for Plymouth City Council*.

WJGL 2023. Pumping Test Factual Report, Phase 2, Bath Street, Plymouth.*Pumping Test Factual Report, Bath Street, Plymouth*. . *Unpublished report to Plymouth City Council*.

Woodcock, N.H., Soper, N.J. and Strachan, R.A. 2007. A Rheic cause for the Acadian deformation in Europe. *Journal of the Geological Society*, **164**, 1023-1036, https://doi.org/doi:10.1144/0016-76492006-129.

Worth, R.N. 1890. *History of Plymouth: From the Earliest Period to the Present Time*. W. Brenden.

WSP. 2021. *Plymouth Geothermal Energy Peer Review Assessment*.

Wyatt, L.M., Parker, K., Mallin Martin, D., Fox, M., Todd, F. and Farr, G. 2025. Drilling into coal mine workings: overview and experience from Britain's coalfields. *Quarterly Journal of Engineering Geology and Hydrogeology*, **58**, https://doi.org/10.1144/qjegh2025-016.

Ziegler, P., Bertotti, G. and Cloetingh, S. 2002. Dynamic processes controlling foreland development–the role of mechanical (de) coupling of orogenic wedges and forelands. *EGU Stephan Mueller Special Publication Series*, **1**, 17-56.

Supplementary Information

SI-1: Photographs of cuttings obtained during the drilling of BHD. Left image shows dark grey, slatey mudstone from 64 to 67mbgl. Right Image shows a pale pink-grey limestone from 79.5 to 80.5mbgl

SI-2: Test Configuration showing location of abstraction well, BHD 'Test Well', location of discharge into culvert and location of culvert egress into Mill Bay Harbour, approximately 500m southwest of the discharge point.

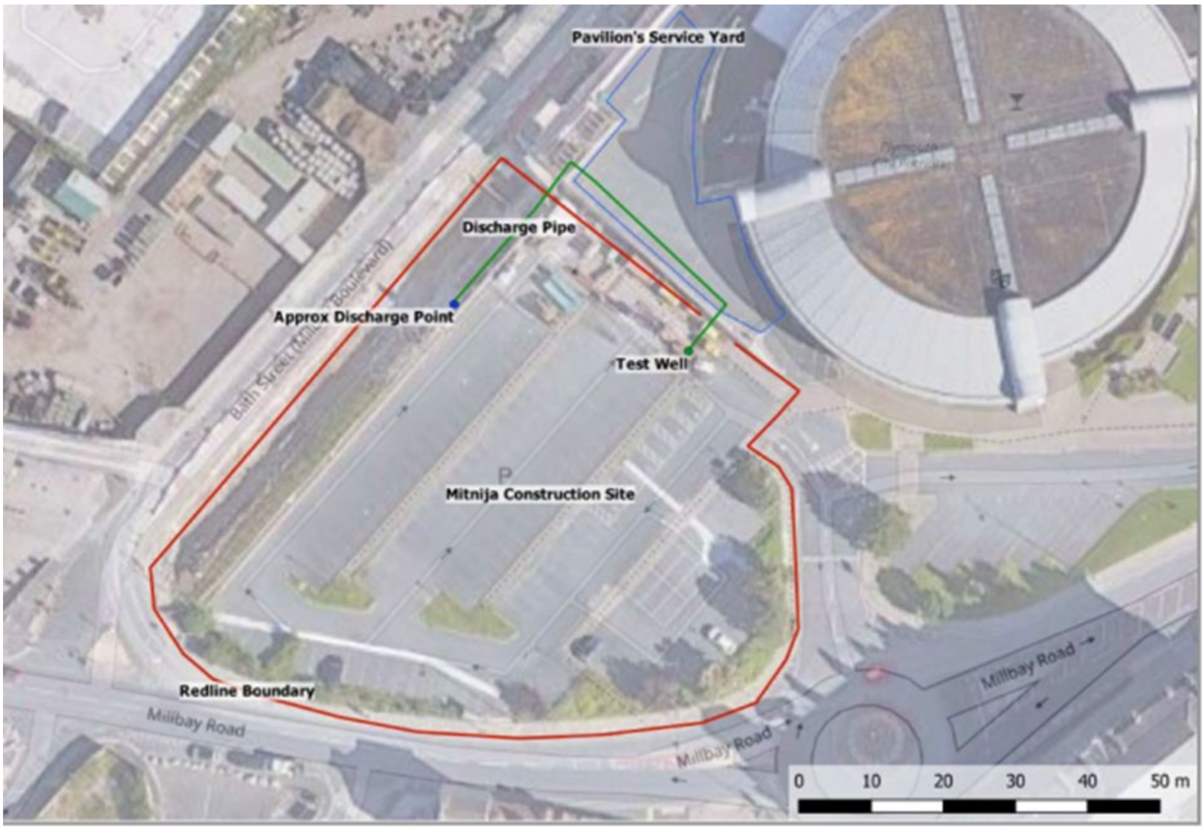

SI-3: Primary scanline survey data. Please see accompanying MS Excel file

SI-4: Screengrab of the Plymouth foreshore from Google Earth (2026) showing part of the area for the large-scale scanline around location 1. Two significant coastal caves can be seen (A and B).

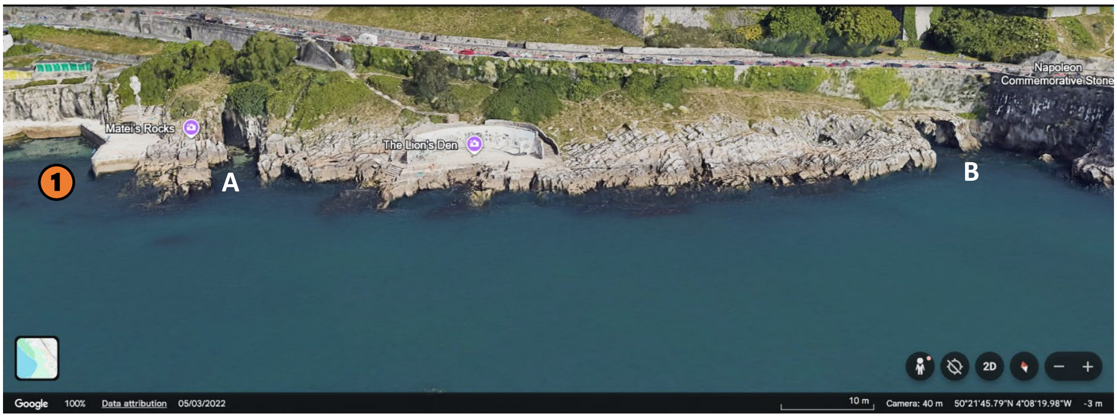

SI-5: Annotated photo of an outcrop at field scanline survey location 2, highlighting the fractures and node type.

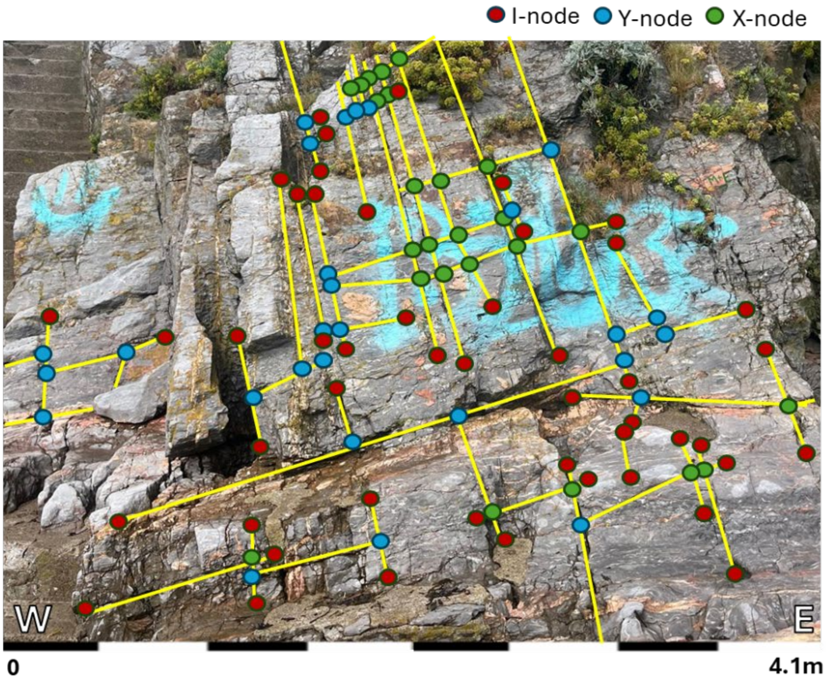

SI-6: Annotated photo of an outcrop at scanline field survey location 3, highlighting the fractures and node type.